Progress in Oceanography 203 (2022) 102780

Contents lists available at ScienceDirect

Progress in Oceanography

journal homepage: www.elsevier.com/locate/pocean

Variability in the meridional overturning circulation at 32°S in the Pacific Ocean diagnosed by inverse box models

Cristina Arumí-Planas [a,*], Alonso Hernández-Guerra [a], Verónica Caínzos [a], Pedro Vélez-Belchí [b], Riccardo Farneti [c], Matthew R. Mazloff [d], Sabine Mecking [e], Isabella Rosso [f], Lena M. Schulze Chretien [g], Kevin G. Speer [h], Lynne D. Talley [d]

[a] Unidad Océano y Clima, Instituto de Oceanografía y Cambio Global, IOCAG, Universidad de Las Palmas de Gran Canaria, ULPGC, Unidad Asociada ULPGC-CSIC, Las Palmas de Gran Canaria, Spain
[b] Centro Oceanográfico de Canarias, Instituto Español de Oceanografía, Santa Cruz de Tenerife, Spain
[c] The Abdus Salam International Centre for Theoretical Physics (ICTP), Trieste, Italy
[d] Scripps Institution of Oceanography, University of California, San Diego, La Jolla, CA, USA
[e] Applied Physics Laboratory, University of Washington, Seattle, WA, USA
[f] GeoOptics Switzerland SA, Lausanne, Vaud, Switzerland
[g] Marine Science Research Institute, Jacksonville University, 2800 University Blvd N, Jacksonville, FL, USA
[h] Department Scientific Computing, Geophysical Fluid Dynamics Institute, Florida State University, Tallahassee, FL, USA

ARTICLE INFO

Keywords:
Physical Oceanography
Climate Change
Global Circulation
Pacific Ocean

ABSTRACT

The meridional circulation and transport at 32°S in the Pacific Ocean in 1992 and 2017 are compared with analogous data from 2003 and 2009 computed by Hernández-Guerra and Talley (2016). The hydrographic data come from the GO-SHIP database and an inverse box model has been applied with similar constraints as in Hernández-Guerra and Talley (2016). In 1992, 2003 and 2017 the pattern of the overturning streamfunction and circulation are similar, but in 2009 the pattern of the circulation changes in the whole water column. The horizontal distribution of mass transports at all depths in 1992 and 2017 resembles the familiar shape of the "classical gyre" also observed in 2003 and is notably different to the "bowed gyre" found in 2009. The hydrographic data have been compared with data obtained from the numerical modelling outputs of ECCO, SOSE, GLORYS, and MOM. Results show that none of these models properly represents the "bowed gyre" circulation in 2009, and this change in circulation pattern was not observed during the entire length of model simulations. Additionally, the East Australian Current in the western boundary presents higher mass transport in the hydrographic data than in any numerical modelling output. Its poleward mass transport ranges from -35.1 ± 2.0 Sv in 1992 to -54.3 ± 2.6 Sv in 2003. Conversely, the Peru-Chile Current is well represented in models and presents an equatorward mass transport from 2.3 ± 0.8 Sv in 2009 to 4.4 ± 1.0 Sv in 1992. Furthermore, the Peru-Chile Undercurrent presents a more intense poleward mass transport in 2009 (-3.8 ± 1.2 Sv). In addition, the temperature and freshwater transports in 1992 (0.42 ± 0.12 PW and 0.26 ± 0.08 Sv), 2003 (0.38 ± 0.12 PW and 0.25 ± 0.02 Sv), and 2017 (0.42 ± 0.12 PW and 0.34 ± 0.08 Sv) are similar, but significantly different from those in 2009 (0.16 ± 0.12 PW and 0.50 ± 0.03 Sv, respectively). To clarify the causes of these different circulation schemes, a linear Rossby wave model is adopted, which includes the wind-stress curl variability as remote forcing and the response to sea surface height changes along 30°S.

1. Introduction

The World Ocean Circulation Experiment (WOCE) was a global oceanographic research program carried out in the 1990s, which assessed every ocean basin with high-quality hydrographic data, from transoceanic zonal and meridional sections of closely spaced stations. The results from this study allowed estimation of the oceanic transports of mass, heat, freshwater and other properties from the sea surface to the seafloor of every ocean (Chapman, 1998; Ganachaud, 2003; Ganachaud and Wunsch, 2000; Macdonald and Wunsch, 1996). As summarized by

* Corresponding author.
E-mail address: cristina.arumi@ulpgc.es (C. Arumí-Planas).

https://doi.org/10.1016/j.pocean.2022.102780
Received 4 October 2021; Received in revised form 3 March 2022; Accepted 7 March 2022
Available online 10 March 2022

Gordon (1986) and Schmitz (1995), the general features of the ocean's global overturning predate WOCE. However, the newly-developed approach of inverse modeling along with the newly collected data, allowed an improved, internally consistent, quantification of global transports (Roemmich and Wunsch, 1985; Wunsch, 1996). From these data, a clear picture of the Meridional Overturning Circulation (MOC) emerged, which is a variable-in-time three dimensional system joining all the ocean basins (Gordon, 1986; Lumpkin and Speer, 2007a,b; Talley, 2003). Therefore, the next step consists of estimating how the property transports and patterns of circulation change over time. In order to accomplish this purpose, repeated hydrographic sections in key latitudes and longitudes have been carried out in the framework of the Global Ocean Ship-Based Hydrographic Investigation Program (GO-SHIP) (www.go-ship.org). Sampling of different ocean properties (including temperature, salinity, nutrients and oxygen) are collected by high accuracy measurements from the surface to the bottom of the ocean with an approximate decadal base, with a spatial resolution according to the internal Rossby radius, and sections that extend from coast to coast or enclose regions. In addition, an inverse method is used to estimate the ocean circulation and property transports from closed hydrographic sections of every ocean (Casanova-Masjoan et al., 2018; Hernández-Guerra et al., 2017, 2005; Hernández-Guerra et al., 2010; Hernández-Guerra et al., 2014, 2019; Hernández-Guerra and Talley, 2016; Pérez-Hernández et al., 2013).

This study is centered at 32°S in the South Pacific Ocean, where the boundary currents in the thermocline layers of the subtropical gyre are the East Australian Current (EAC) in the western boundary, and a set of eastern boundary flows alternating in the north/south direction: the equatorward Peru-Chile Current and the poleward Peru-Chile Undercurrent. The EAC is the intense western boundary current flowing along the east Australian shelf break and slope as part of the anticyclonic circulation of the south Pacific gyre (Hamon and Tranter, 1971; Tomczak and Godfrey, 1994). The presence of New Zealand, near 34°S, distorts the circulation in the southern limb (Godfrey, 1989), causing the EAC to separate from the Australian coast and to flow eastward, with its southern boundary forming a strongly eddying feature: the Tasman Front (Mulhearn, 1987). The Peru-Chile Current is the wide eastern boundary current, flowing northward along the upper waters off the west coast of South America. The Peru-Chile Undercurrent is a subsurface current flowing poleward over the slope along the Peruvian and Chilean coasts (Strub et al., 1998). The Indonesian Throughflow (ITF) is the main gateway of upper layer waters from the Pacific Ocean transported westward into the surface waters of the Indian Ocean (Hernández-Guerra and Talley, 2016).

The main goal of this work is to extend a previous study of the Pacific Ocean at 32°S carried out by Hernández-Guerra and Talley (2016), which was focused on the 2003 and 2009 sections, as well as to estimate the changes of the ocean circulation across different decades, by analyzing and comparing hydrographic data collected in 1992 and in 2017, together with those in 2003 and 2009. Furthermore, an attempt to infer the dynamical forcing causing the change in ocean circulation is carried out. To accomplish these goals, Section 2 presents the hydrographic and numerical model data used in this study. Section 3 exhibits the vertical sections of the different ocean properties to describe the main water masses present at 32°S. Next, Section 4 describes the geostrophic transport relative to the reference level, followed by the characteristics of the inverse model. The final mass and silicate transports obtained after applying the inverse model are described in Section 5, including the estimate of the meridional overturning circulation and its change in time. Section 6 describes the horizontal circulation focusing on the upper, deep, and abyssal layers with a specific study of the EAC and the Peru-Chile Current and Undercurrent. Section 7 shows a comparison between the hydrographic data and output of numerical model data with the aim of studying if the circulation changes are reproduced by these models. Section 8 presents the Sea Surface Height Anomaly and Rossby wave dynamics as responsible of the circulation variability at 30°S in the South Pacific Ocean. Section 9 shows the temperature and freshwater transports for the four hydrographic realizations, and finally, a discussion with the conclusive remarks is provided in Section 10.

2. Hydrographic and numerical model data

Hydrographic data collected in 1992 (02/05–13/07) and 2017 (03/07–30/09) over the entire water column at stations along section P06 at nominally 32°S in the South Pacific Ocean area added to the surveys done in 2003 (03/08–16/10) and 2009 (21/11–10/02) (Fig. 1). Previous studies carried out by Ganachaud (2003) and Hernández-Guerra and Talley (2016) have already analyzed the data compiled in 1992, and 2003 and 2009, respectively. In this study, we have again processed and analyzed the 1992 data. All these data were collected as part of the WOCE and GO-SHIP (Talley et al., 2016), and are publicly available through the CLIVAR and Carbon Hydrographic Data Office (CCHDO, http://cchdo.ucsd.edu) (Table 1).

Additionally, SADCP data for 2017, collected using a 38 kHz narrowband RDI system were used for geostrophic velocity referencing, complemented by some LADCP station profiles. A system formed by an upward-looking (300 kHz) and a downward-looking (150 kHz) LADCP was used to provide a velocity profile from the surface to the bottom of the ocean at each station. The LADCP data were processes using the LDEO Matlab package, using the bottom track (BT) and ship drift (GPS) constraints and blending the SADCP data with LADCP data (https://currents.soest.hawaii.edu/go-ship/ladcp_rst_2015-2018/2017_P06_ancillary-data.html#ancillary-data-2017-p06). Fig. 3 shows the velocity profiles of LADCP and SADCP, which sometimes don't match. This profile of SADCP is computed as the average velocity from one station to the next station, while the SADCP used to compute the LADCP velocities are the SADCP in each hydrographic station. As geostrophy integrates the velocity between stations, LADCP velocities on each station fail to resolve the horizontal sampling due to the fact that they are located in each station and not in the middle as geostrophic velocity is calculated. However, the continuous underway SADCP data set can be used to average between stations, so it matches the integration in geostrophy (E. Firing, personal communication). For this reason, SADCP data are expected to be a more useful tool to estimate the velocity at the reference level.

We complement our hydrographic data with simulations from a set of ocean models, as follows.

The Geophysical Fluid Dynamics Laboratory (GFDL) OM4 ocean/sea ice model is used (Adcroft et al., 2019). The ocean component of OM4 uses version 6 of the Modular Ocean Model (MOM, hereafter) and has a nominal 0.25° horizontal spacing with no mesoscale eddy parameterization and 50 vertical levels. The dynamical core of MOM is based on the hydrostatic primitive equations formulated in their generalized vertical coordinate form. MOM was forced with the JRA55-do atmospheric reanalysis product (Tsujino et al., 2020) over the years 1958–2018 and monthly averages were stored for the entire length of the simulation.

ECCOv4r3 (Estimating the Circulation and Climate of the Ocean Version 4 Release 3; ECCO, hereafter) is a data-assimilating model produced by the Jet Propulsion Laboratory. ECCOv4r3 includes monthly data of the state of ocean's evolution over time for the period 1992–2015 with a nominal 1° horizontal resolution configuration of the MIT general circulation model over the entire globe (Forget et al., 2015; Fukumori et al., 2017).

The Southern Ocean State Estimate (SOSE) is a sea ice-ocean data-assimilating model developed at the Scripps Institution of Oceanography which provides a monthly gridded dataset at 1/6° horizontal resolution for the period 2005–2010. While this model does not come with explicit uncertainty estimates, the major biases are well documented and include too-shallow pycnocline in the subpolar gyres and too broad of a range in mixed-layer depth (Mazloff & National Center for Atmospheric

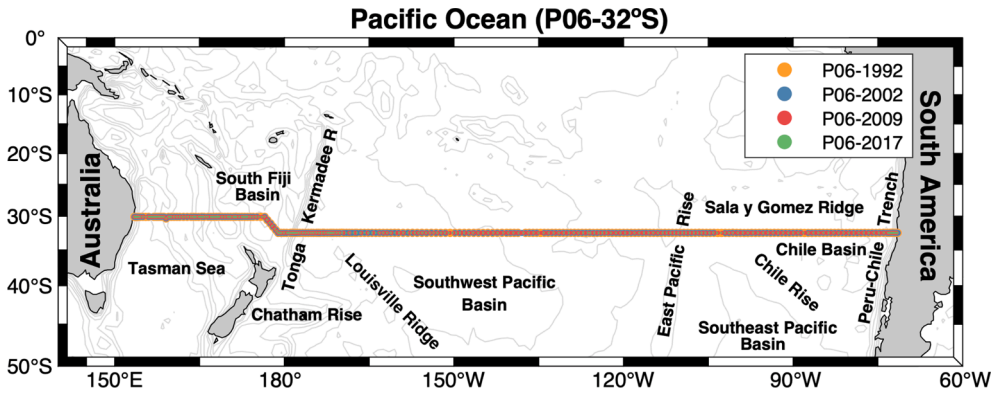

Fig. 1. Station positions for P06 cruises carried out at nominally 32°S in the Pacific Ocean in 1992, 2003, 2009, and 2017.

Table 1
Hydrographic cruise information. All CTD data are available online from the CLIVAR and Carbon Hydrographic Data Office (CCHDO, http://cchdo.ucsd.edu/). In 2017, LADCP and SADCP data for P06-West and P06-East are available online from the CLIVAR archive https://usgoship.ucsd.edu/cruise-data-submit-download/.

Cruise	Dates	No. stations	CCHDO Expocode	Ship	Chief scientist
P06-East	1992-05-02 to 1992-05-26	69	316N138_3	KNORR	H. L. Bryden (Woods Hole Oceanographic Institution, Woods Hole, MA 02543, USA)
P06-Center	1992-05-30 to 1992-07-07	114	316N138_4	KNORR	M. McCartney (Woods Hole Oceanographic Institution, Woods Hole, MA 02543, USA)
P06-West	1992-07-13 to 1992-07-30	78	316N138_5	KNORR	J. Toole (Woods Hole Oceanographic Institution, Woods Hole, MA 02543, USA)
P06-West	2017-07-03 to 2017-08-17	143	320,620,170,703	Nathaniel B. Palmer	S. Mecking (Applied Physics Laboratory, University of Washington, USA)
P06-East	2017-08-20 to 2017-09-30	107	320,620,170,820	Nathaniel B. Palmer	K. Speer (Department of Oceanography, The Florida State University, USA)

Research Staff (Eds.), 2016.).

The CMEMS (Copernicus Marine Environment Monitoring Service) ocean model GLORYS12V1 (Global Ocean Physics Reanalysis; GLORYS, hereafter) is a global ocean reanalysis at eddy-resolving resolution describing ocean circulation, including forcing by satellite altimetry measurements of sea level from the period 1993–2019. It is based on the current real-time global forecasting CMEMS system. The model hydrodynamics are based on NEMO (Nucleus for European Modelling of the Ocean). In situ observations are assimilated from CORA4 database, and atmospheric forcing from ERA-Interim data. Furthermore, altimeter data (sea level anomaly), satellite sea surface temperature, sea ice concentration, and in situ temperature and salinity vertical profiles are jointly assimilated. The monthly gridded datasets are displayed on a standard regular grid at 1/12° (~8 km) and on 50 standard levels (Drévillon et al., 2018).

In summary, three of the models used (ECCO, SOSE and GLORYS) are data-assimilating models spanning from coarse to eddy-permitting horizontal resolution (1°, 1/6° and 1/12°), and the fourth one (MOM) is a free-running model with a relatively high horizontal resolution (1/4°). Also, the models have been run over different periods of time with at least two model outputs available for each P06 occupation. Monthly data over the entire water column along 30°S in the South Pacific Ocean for June 1992 (MOM and ECCO), September 2003 (MOM, ECCO, and GLORYS), January 2010 (MOM, ECCO, SOSE, and GLORYS), and August 2017 (MOM and GLORYS) are compared with the mass transports from hydrographic data after the inverse model is applied. The latitude chosen for the models is 30°S in order to match the western part of the P06 section. With this choice, the EAC is better represented and there are no major changes between the circulation in the ocean interior between 30°S and 32°S.

3. Vertical sections and water masses

Transpacific vertical sections of potential temperature, salinity, neutral density γ^n (Jackett and Mcdougall, 1997), oxygen and silicate at the P06 nominal latitude of 32°S are used to identify the existing water masses in the South Pacific Ocean (Fig. 2), following Talley et al. (2011). Fig. 2 shows the labels of the water masses.

In the upper layer, between the surface and$\gamma^n = 26.45$ kg/m^3 (above ~ 200 m depth), the South Pacific Central Water (SPCW) is found with relatively high potential temperature (>15 °C, Fig. 2a), relatively high salinity (>34.5, Fig. 2b) and high dissolved oxygen and low silicate values (>220 μmol/kg and < 2 μmol/kg, Fig. 2c and d respectively). This water mass is characterized by subtropical thermocline waters formed by subduction (Talley et al., 2011). The SPCW can be divided into two different water masses: Western South Pacific Central Water (WSPCW) and Eastern South Pacific Central Water (ESPCW). The WSPCW (S > 35.5 and dissolved oxygen ~ 230 μmol/kg) is separated from the eastern boundary by the fresher ESPCW (34.5 < S < 35 and dissolved oxygen ~ 230–250 μmol/kg) (Emery, 2001; Emery and Meincke, 1986; Sprintall and Tomczak, 1993).

In the western boundary, the South Pacific Subtropical Mode Water (SPSTMW) is found below the WSPCW to roughly$\gamma^n = 27.00$ kg/m^3, which corresponds to ~ 300–600 m depth. SPSTMW is formed by the subduction of thick winter mixed layer and characterized in the vertical by low levels of dissolved oxygen (<200 μmol/kg, Fig. 2c), salinities of ~ 35–35.5 (Fig. 2b), and potential temperatures of about 10–19 °C (Fig. 2a).

The Equatorial Subsurface Water (ESSW), found in eastern coastal regions between 26.45 kg/m^3<γ^n < 27.00 kg/m^3 (~300–500 m depth), is formed near the equator by vertical mixing of waters. The ESSW is carried eastward by the Equatorial Undercurrent and the Southern Subsurface Countercurrent, and then the Peru-Chile Undercurrents transport ESSW southward to approximately 48°S (Montes et al., 2010;

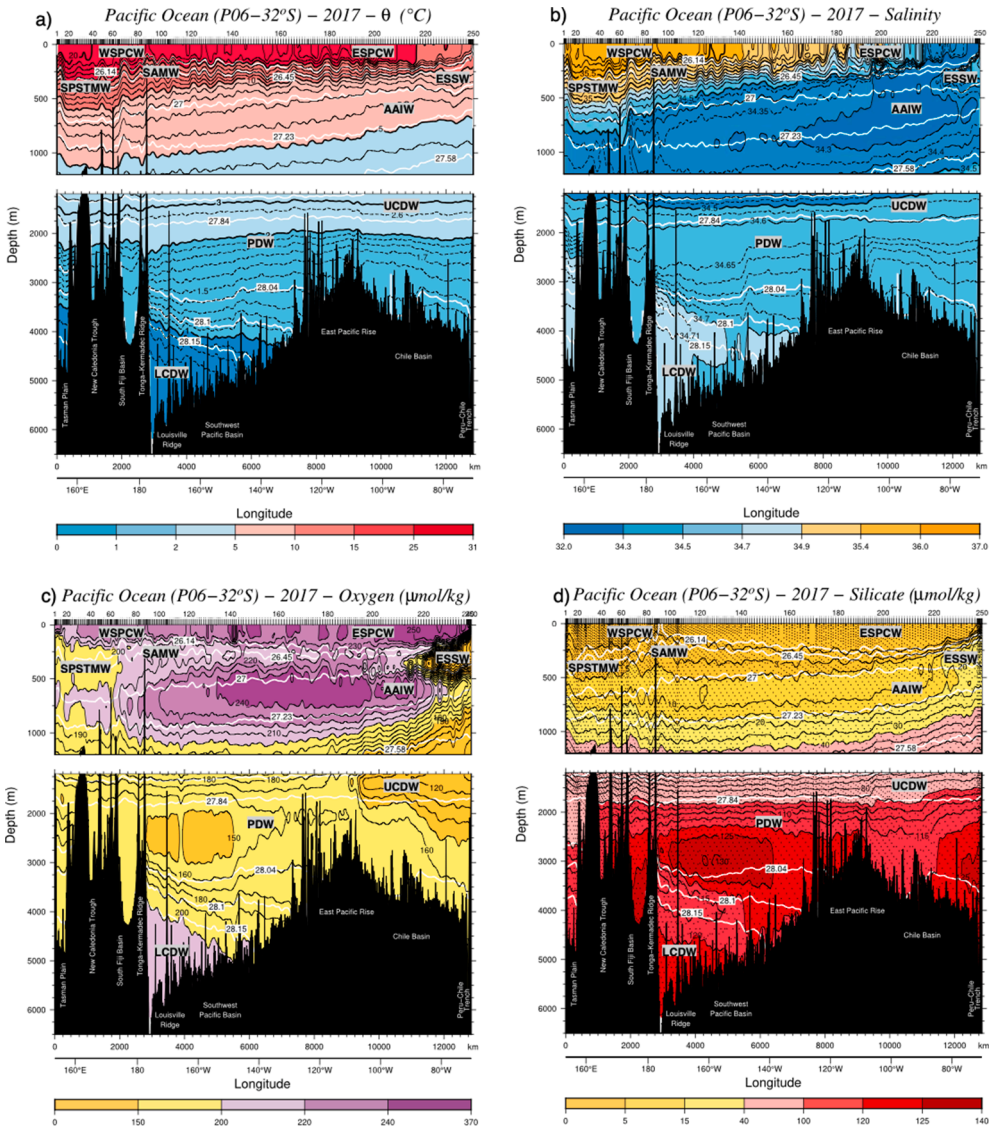

Fig. 2. Vertical sections of (a) θ (°C), (b) salinity, (c) oxygen (μ mol/kg), and (d) silicate (μ mol/kg) at 32°S in the Pacific Ocean for data collected in 2017. The water masses identified are: Eastern South Pacific Central Water (ESPCW), Western South Pacific Central Water (WSPCW), South Pacific Subtropical Mode Water (SPSTMW), Equatorial Subsurface Water (ESSW), Subantarctic Mode Water (SAMW), Antarctic Intermediate Water (AAIW), Upper Circumpolar Deep Water (UCDW), Pacific Deep Water (PDW), and Lower Circumpolar Deep Water (LCDW). Tick-marks on the top axis indicate the location of stations. The isoneutrals labeled (white lines) are the γ^n layers used to estimate the geostrophic transport.

Neshyba, 1979; Stramma et al., 2010; Tsuchiya and Talley, 1998; Wyrtki, 1967). ESSW is characterized by potential temperatures of about 6–10 °C (Fig. 2a), relatively low salinities (>34.3, Fig. 2b), silicate concentrations of > 10 μmol/kg (Fig. 2d), and extremely low oxygen values (<150 μmol/kg, Fig. 2c) (Brink and Robinson, 2005; Silva et al., 2009).

The Subantarctic Mode Water (SAMW) is found between 26.45 kg/m^3<γ^n < 27.00 kg/m^3, which corresponds to ~ 300–500 m depth. SAMW is formed by subduction of thick winter mixed layer from Subantarctic Front and is characterized in the vertical by potential temperatures of about 10–15 °C (Fig. 2a), relatively high salinities (~35–35.5, Fig. 2b), oxygen values of about 200 μmol/kg (Fig. 2c), and low silicate concentrations (<5 μmol/kg, Fig. 2d).

Below this layer, in the intermediate waters (between 27.00 kg/m^3<γ^n < 27.58 kg/m^3, which corresponds to ~ 500–1500 m depth) the Antarctic Intermediate Water (AAIW) is located. The AAIW is formed by advection of fresh Subantarctic Surface Waters (SASW). The AAIW is a relatively cold water mass with potential temperatures of about 4–8 °C (Fig. 2a), and it is characterized in the vertical by the minimum salinity values (<34.4, Fig. 2b), high dissolved oxygen concentration (>200 μmol/kg, Fig. 2c), and a silicate concentration of ~ 5–50 μmol/kg (Fig. 2d) (Talley et al., 2011; Tsuchiya, 1990; Tsuchiya and Talley, 1996).

In the deep layer, with a neutral density range of 27.84 kg/m^3<γ^n < 28.10 kg/m^3, extending in the range ~ 1500–4000 m depth, is found the core of the Pacific Deep Water (PDW), which is formed by mixing and aging of deep waters that flow into the Southern Ocean. Because of its formation mechanism and source, the waters in the PDW are the oldest of the global ocean. The PDW is characterized in the vertical by low levels of oxygen (<200 μmol/kg, with a minimum of 150 μmol/kg in the ocean interior, Fig. 2c), low potential temperatures (1–3 °C, Fig. 2a), salinity values of about 34.5–34.7 (Fig. 2b), and the maximum silicate concentration among the different water masses (about 70–130 μmol/kg, Fig. 2d) (Knauss, 1962; Talley et al., 2011; Wijffels et al., 2001).

In the South Pacific, the core of the Upper Circumpolar Deep Water (UCDW) is located in shallower layers (27.58 < γ^n < 28.04 kg/m^3) than the core of the PDW. The UCDW is formed by the mixing of deep waters in the Southern Ocean, and is characterized in the vertical by low levels of oxygen (<160 μmol/kg, Fig. 2c), low potential temperatures (~1.4–4 °C, Fig. 2a), a silicate concentration of about 40–125 μmol/kg (Fig. 2d), and salinity values of ~ 34.4–34.69 (Fig. 2b) (Callahan, 1972; Talley et al., 2011).

The densest water mass in the Pacific, γ^n>28.1 kg/m^3 from approximately 4000 m depth to the seafloor, is called the Lower Circumpolar Deep Water (LCDW). The analogous layer in the Atlantic is commonly called Antarctic Bottom Water (AABW). As stated in Talley

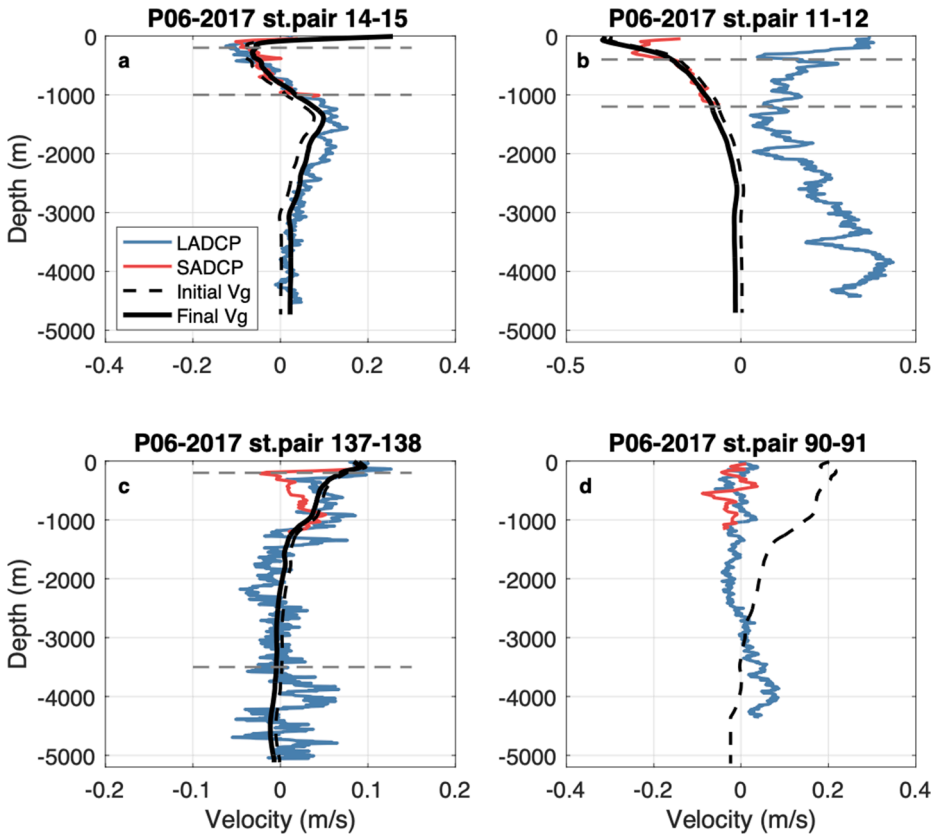

Fig. 3. Comparison between the initial geostrophic velocity profile (dashed black lines), the LADCP (blue line) and SADCP (red line) velocity normal to the station pairs, and the geostrophic velocity adjusted with LADCP or SADCP data (black solid line). The subplots correspond to different adjustment examples: (a) both, SADCP and LADCP, data agree with the geostrophic velocities, (b) only SADCP data agree, (c) only LADCP data agree, and (d) none agree.

et al. (2011), this water mass comes from the Southern Ocean formed by a mixture of the deep waters of all three Oceans: North Atlantic Deep Water (NADW), PDW and Indian Deep Water (IDW). LCDW is identified in the Pacific Ocean by low potential temperatures (<1°C, Fig. 2a) and high salinity (>34.7, Fig. 2b). Moreover, if compared with PDW, the higher oxygen concentration (~200 μmol/kg, Fig. 2c) and lower silicate concentration (~120 μmol/kg, Fig. 2c) of the LCDW, indicate that it is significantly younger than the PDW (Kawano et al., 2006; Talley et al., 2011).

In addition, the tilted isotherms and isoneutrals in the transpacific vertical sections allow to identify the effect of the East Australian Current (EAC) in the western basin, and the Peru-Chile Current (PCC) in the eastern basin and the Deep Western Boundary Current (DWBC) on the eastern flank of the Tonga-Kermadec Trench (Fig. 2).

4. Relative geostrophic transport and inverse model

Geostrophic velocity and transport are calculated using temperature-salinity profiles collected at each station pair along section P06 in 1992, previously computed by Ganachaud (2003), and in 2017 (Fig. 1). The distance between stations takes into account the internal Rossby radius, with smaller spacing across boundary currents and across strong topographic slopes, both in the interior and close to the coasts. At each station, the temperature and salinity every two decibars were collected for the full water column depth using a SeaBird 911 + Conductivity-Temperature-Depth (CTD), as well as water samples for salinity, oxygen, silicate, and other chemical tracers.

The thermal wind equation is used to compute the relative geostrophic velocity profile at each station pair, with a reference layer of no motion chosen at the neutral density $\gamma^n = 28.1$ kg/m^3 that separates the deep and the abyssal waters (Fig. 2). This layer, also known as ZVS "Zero Velocity Surface", is the same used in previous studies carried out using hydrographic data at 30°S in the Pacific Ocean (Ganachaud, 2003; Hernández-Guerra and Talley, 2016; Hernández-Guerra et al., 2019). If the deepest common level of the stations pairs is shallower than the reference layer, the bottom is used as the initial reference level of no motion. Below the deepest common depth of each station pair, velocities are considered to be constant. In addition, the velocities at the reference level are estimated from Lowered Acoustic Doppler Current Profiler (LADCP) and Shipboard Acoustic Doppler Current Profiler (SADCP) data from the 2017 occupation (Comas-Rodríguez et al., 2010; Joyce et al., 2001; Wijffels et al., 1998). Finally, the velocities at the reference level are adjusted from an inverse box model for 1992 and 2017, in which only the mass and silicate transports were used. For the inverse model, the same constraints as in Hernández-Guerra and Talley (2016) have been used to be able to compare both results.

Fig. 3 shows a comparison between the initial geostrophic velocity (dashed black lines), the SADCP velocity averaged between stations (red line), LADCP velocity (blue line) calculated as the mean of the LADCP velocities in each hydrographic station, and the geostrophic velocity adjusted to the SADCP or LADCP velocity (black solid line), with four different adjustments. Firstly, either if both LADCP and SADCP (Fig. 3a) or just the SADCP data agree (Fig. 3b) with the profile of the geostrophic velocity, the initial geostrophic velocity is adjusted to the SADCP data. Secondly, if only the LADCP data agrees with the pattern of the geostrophic velocity, the initial geostrophic velocity is adjusted to LADCP data (Fig. 3c). If neither the structure of the LADCP nor SADCP data agree with the profile of geostrophic velocity, the initial geostrophic velocity is not adjusted (Fig. 3d).

Following Hernández-Guerra and Talley (2016), Hernández-Guerra et al. (2019) and Talley (2008), mass and property transports are computed for the different isoneutral layers that divide the water

column (Fig. 2). The surface geostrophic transport includes the net Ekman transport into the first layer in both 1992 and 2017. The Ekman transport is computed using the NCEP (National Centers for Environmental Prediction) wind-stress (Kalnay et al., 1996) corresponding to the time of the cruise following Hernández-Guerra and Talley (2016). The resulting surface winds for the cruise periods give an Ekman transport of 0.31 ± 0.16 Sv and 0.33 ± 0.16 Sv for 1992 and 2017, respectively (1 Sv = 10^6 $m^3/s \approx 10^9$ kg/s). The inverse model adjusts these initial Ekman transports to 0.31 ± 0.16 Sv and 0.29 ± 0.15 Sv for 1992 and 2017, respectively.

The initial zonally-integrated mass and silicate transports per layer through 32°S in the Pacific Ocean are shown in Fig. 4. The initial mass and silicate transport include the estimation of the velocity at the reference layer from ADCP data. The total mass transport presents a northward initial imbalance of 7.1 Sv for 1992 and of 26.3 Sv for 2017 (Table 2). The circulation schema presents an equatorward mass transport for the upper and bottom layers, and a southward mass transport at deep layers. The initial silicate transport structure is similar to the mass transport and presents a northward initial imbalance of −689.6 kmol/s and of 801.4 kmol/s for 1992 and 2017 (Table 2), respectively.

In order to reduce this large imbalance, an inverse model has been applied to estimate an adjustment to the velocity at the reference layer, subject to chosen constraints and uncertainties (Wunsch, 1978, 1996). The subsequent equation for mass transport must be solved:

$$\iint \rho b dx dz = -\iint \rho V_r dx dz + E_k$$

where ρ is the density, b is the unknown reference velocity, V_r is the relative geostrophic velocity obtained from the thermal wind equation with the estimated referenced velocities from ADCP data, E_k is the Ekman transport normal to the section, and x and z designate the along-section and vertical coordinates, respectively. See the Appendix A to know how to introduce the ITF and Bering Strait transport constraints.

For silicate transport, the above equation has to be multiplied for the silicate concentration.

This procedure provides one single equation for each vertically integrated mass and silica constraint with 228 and 248 unknowns (the number of station pairs) for 1992 and 2017, respectively. The silicate transport constraint applied in this study differs from the no net meridional silica transport previously applied in the inverse model by Hernández-Guerra and Talley (2016), Robbins and Toole (1997), and Wijffels et al. (2001). This study uses a more recent silicate transport constraint estimated by Talley and Sprintall (2005). In addition to total mass and silica constraints, several regional constraints were introduced for different longitude and depth ranges (Table 2). Previous studies of earlier occupations of these sections in the Pacific (Hernández-Guerra and Talley, 2016; Wijffels et al., 2001) included the same mass transport constraints in specific longitude ranges and depths from independent data. Thus, equatorward mass transport for the narrow Deep Western Boundary Current (DWBC) just east of the Tonga-Kermadec Ridge (TKR) is constrained (Whitworth et al., 1999).

The solution of the inverse model follows the same approach developed in Joyce et al. (2001) and subsequently carried out by Casanova-Masjoan et al. (2018) and Casanova-Masjoan et al. (2020), with some specific differences. The closed box for the inverse model is composed of the transpacific 32°S section plus the ITF and Bering Strait transport. The full matrix equation and its derivation are provided in the Appendix A. Following Wunsch (1996), the inverse problem is solved through the Gauss–Markov method, which requires *a priori* variance for each equation and solution chosen to be the same as in Hernández-Guerra and Talley (2016). The *a priori* velocity variance for the solution is set to $(2\ cm/s)^2$, except in regions with strong shear that increases to $(4\ cm/s)^2$, corresponding to the EAC and the DWBC. The *a priori* variance expressed as standard deviation of each equation is shown in Table 2. The Gauss–Markov method solves an undetermined system of equations by choosing the one that minimizes its variance, providing the

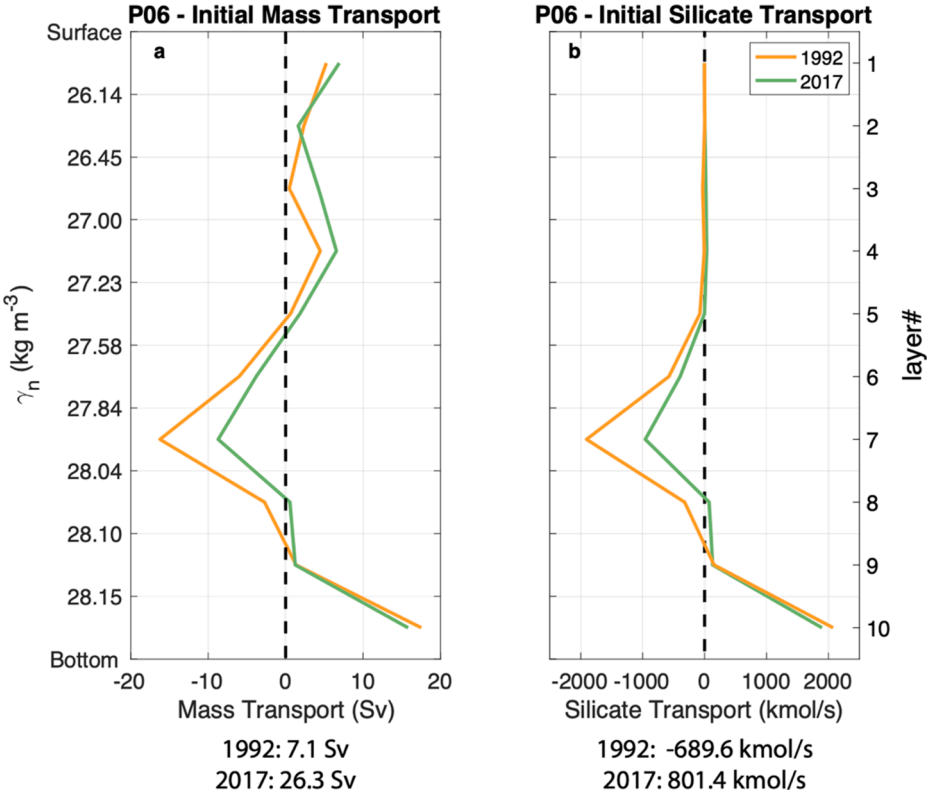

Fig. 4. Initial zonally-integrated meridional mass (Sv) (a) and silicate transport (kmol/s) (b) per layer across 32°S in the Pacific Ocean for data collected in 1992 and in 2017.

Table 2
Regional transport constraints and inverse model results for the Pacific Ocean (P06) at 32°S in 1992 and 2017. Positive transports are northward, and negative are southward. Initial and final transports relative to the ZVS at $\gamma^n = 28.1$ kg/m^3 are listed.

Pacific Ocean - P06	Property	Longitude	Layers	Constraint	1992 Initial	1992 Final	2017 Initial	2017 Final
Total mass[a]	ITF and Bering Strait transport (Sv)	All	1:10	15 ± 5	7.1	15.2 ± 10.3	26.3	15.3 ± 10.4
Silicate conservation[b]	Total Silicate (kmol/s)	All	1:10	120 ± 20	−689.6	120.4 ± 1166	801.4	0.1 ± 256
Deep transport[c]	Tasman Sea (Sv)	150–161°E	9:10	0.5 ± 0.5	0.2	0.75 ± 1.0	0.1	1.2 ± 0.5
Deep transport[c]	Tasman Sea (Sv)	161–173°E	7:10	0 ± 0.5	0.4	0.0 ± 0.5	1.2	0.0 ± 0.5
Deep transport[c]	Tasman Sea (Sv)	173–181°E	7:10	0 ± 0.5	−1.0	−0.0 ± 0.6	1.5	0.0 ± 0.5
Deep transport[c]	Eastern Basin (Sv)	110–70°W	8:10	0.75 ± 0.75	−1.0	0.7 ± 0.7	−0.8	0.7 ± 0.7
DWBC constraint[d]	Tonga-Kermadec Ridge (Sv)	180–168°W	8:10	15 ± 4	10.8	14.8 ± 4.7	13.5	13.5 ± 3.1
Boundary current result	East Australian Current (Sv)	Coast to 154.3°E (1992) 156.6°E (2017)	1:8	NA	NA	−35.1 ± 2.0	NA	−39.2 ± 1.6
Boundary current result	East Australian Current Recirculation (Sv)	154.3° to 156.7°E (1992) 156.6° to 158.5°E (2017)	1:8	NA	NA	17.2 ± 1.9	NA	12.3 ± 2.5
Boundary current result	Peru-Chile Current (Sv)	85°W to coast	1:3	NA	NA	4.4 ± 1.0	NA	4.4 ± 0.8
Boundary current result	Peru-Chile Undercurrent (Sv)	75°W to coast	4:5	NA	NA	–	NA	−1.5 ± 0.8
Boundary current result	Deep Eastern Boundary Current	76.3°W to coast (1992) 86.0°W to coast (2017)	6:7	NA	NA	−6.9 ± 4.9	NA	−8.5 ± 6.8

[a] ITF transport from Gordon et al. (2010) and Sprintall et al. (2009).
[b] Silicate conservation from Talley and Sprintall (2005).
[c] Deep transport constraints from Wijffels et al. (2001).
[d] DWBC constraint from Whitworth et al. (1999).

velocities at the reference layer together with their uncertainties. From here, we have estimated mass transports and uncertainties.

The velocities at the reference level estimated from SADCP and LADCP data and from the inverse model for 2017 are presented in Fig. 5. The adjusted velocities from ADCP data (Fig. 5a) are higher than the velocities from the inverse model (Fig. 5b), which are not significantly different from zero (i.e. −0.02 ± 0.08 cm/s) at all stations as in previous inverse models (Hernández-Guerra and Talley, 2016; Hernández-Guerra et al., 2019).

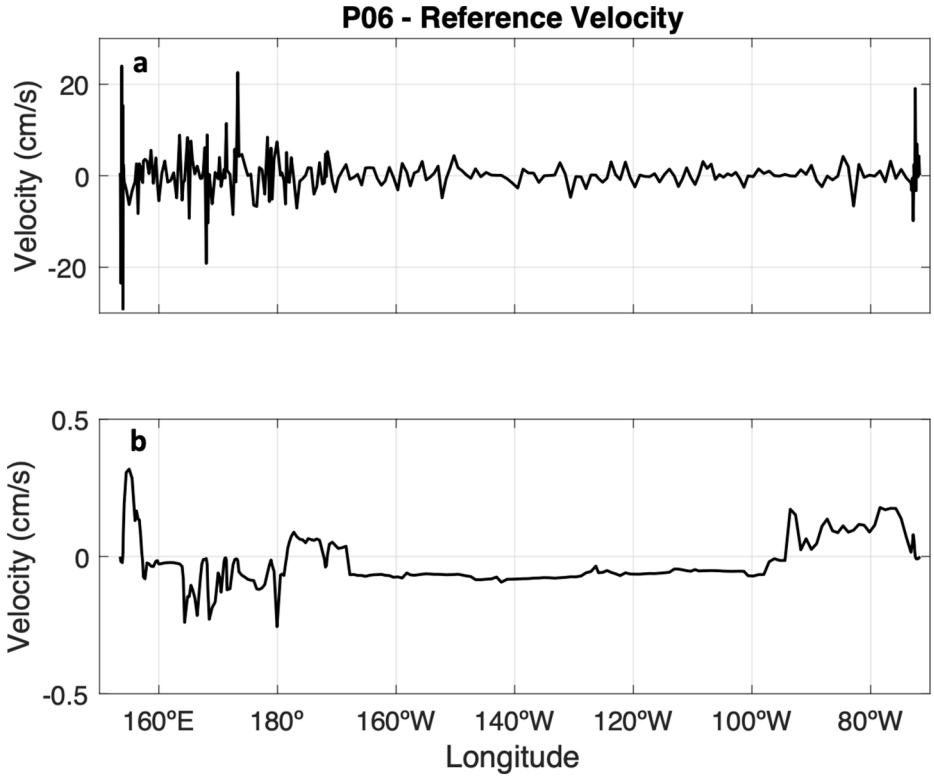

Fig. 5. Geostrophic velocity (cm/s) adjusted to the SADCP or LADCP data (a) and reference velocities from the inverse model (b) at each station pair for 2017 P06 section at nominally 32°S in the Pacific Ocean.

5. Final adjusted transport

5.1. Meridional transport per layer

Fig. 6 shows the final mass and silicate transports per neutral density layer after the inverse model, where both mass and silicate transports from Hernández-Guerra and Talley (2016) for 2003 and 2009 are included, is applied. For both 1992 and 2017, the net initial mass (7.1 and 26.3 Sv, respectively) and silicate transports imbalances (-689.6 kmol/s and 801.4 kmol/s, respectively) are adjusted to the constraints (15.2 ± 10.3 Sv and 15.3 ± 10.4 Sv, and 120.4 ± 1166 kmol/s and 0.1 ± 256 kmol/s, in 1992 and 2017, respectively) as seen from the total transports in Table 2. Thus, the final transports satisfy the constraints within the uncertainty. The total mass transport for 1992 is comparable with the mass transport 16.1 ± 5.1 Sv estimated from the inverse model developed by Ganachaud (2003). Results show the same pattern as previous analyses of the mass transport per layer at this latitude for 2003 and 2009 (Hernández-Guerra and Talley, 2016), with a roughly similar transport pattern in 1992, 2003, 2009 and 2017: northward mass transport in the upper (Layers 1–5) and abyssal layers (Layers 9–10), and southward mass transport in the deep layers (Layers 6–8). In 2017, layer 8 has a slight northward mass transport probably due to warming of the abyssal layers (Purkey et al., 2019), but it has been included in the deep layers according to its density following Hernández-Guerra and Talley (2016).

Inverse model results show that abyssal equatorward flow in the transoceanic section at 32°S is bottom intensified (Fig. 6), with a northward flow of 20.5 ± 6.7 Sv and 16.1 ± 7.8 Sv for 1992 and 2017, respectively. This bottom Pacific mass transport is consistent with previous estimates. For the 32°S WOCE section, Wijffels et al. (2001) estimated a similar net northward inflow of 18 ± 2 Sv. Weaker net equatorward mass transports were estimated by Wunsch et al. (1983) (12 Sv in the lowest layers) using the 1968 Scorpio sections. Using Reid (1997)'s absolute geostrophic velocity for the Scorpio sections. Talley et al. (2003) estimated a deep inflow of 10 Sv, and Katsumata and Fukasawa (2011) obtained a Pacific deep inflow of 10 Sv below γ^n = 28.0 kg/m^3, which was larger than their 8 Sv result for the 1992 WOCE occupation. A more moderate inflow of 7 ± 2 Sv at 32°S in 1992 was estimated with a global inverse model by Ganachaud and Wunsch (2000). More recently, with a global inverse model, Lumpkin and Speer (2007a,b) presented a stronger inflow of 14.9 ± 3.4 Sv. Most recently, Hernández-Guerra and Talley (2016) estimated a net equatorward deep inflow of 15.5 ± 6.9 Sv for 2003 and 10.8 ± 6.5 Sv for the 2009 GO-SHIP section, which are not significantly different from our results for 1992 and 2017.

The deep and bottom layers of the adjusted silicate transport (Fig. 6b) resemble the profile of mass transport (Fig. 6a). There is a northward silicate transport in the deepest layers (Layers 8–10), as well as a poleward silicate transport in the deep layers (Layers 6–7) that extends up to layer 5. Low silicate transports in the uppermost layers (Layers 1–4) result from very low silicate values in the first 1000 m of the water column (Fig. 2d and 6b). Once again, silicate transports resemble the profile of 2003 and 2009 results computed by Hernández-Guerra and Talley (2016), with a roughly similar silicate transport pattern in years 1992, 2003, 2009 and 2017.

5.2. Meridional overturning transport

The meridional overturning transport across 32°S for the Pacific Ocean is computed by vertically integrating the mass transport from the bottom to the surface of the ocean (Fig. 7). The resulting overturning streamfunction for 2003 and 2009, computed by Hernández-Guerra and Talley (2016) and reproduced in Fig. 7, presents a nearly zero net flow in layer 3. Such characteristic may be caused by the balance between net northward flow for the ITF and net southward flow in the thermocline associated with the shallow overturn of the subtropical gyre (Talley,

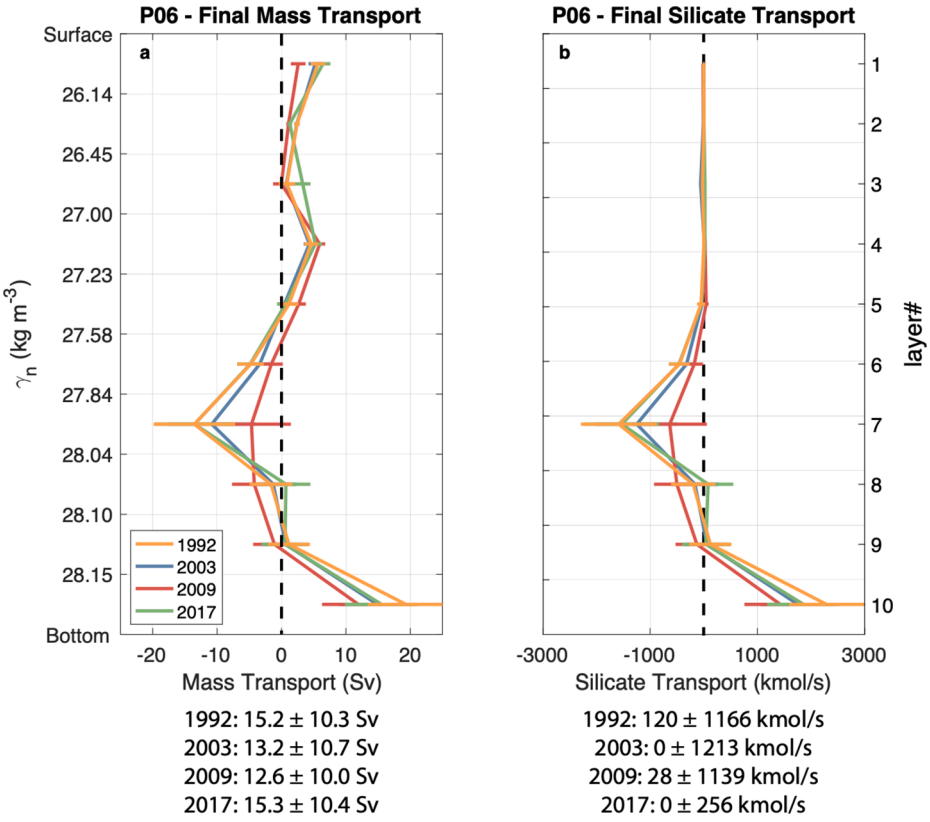

Fig. 6. Final zonal-integrated meridional mass transport (Sv) (a) and silicate transport (kmol/s) (b) per layer, with error bars, across 32°S in the Pacific Ocean for data collected in 1992, 2003, 2009 and 2017.

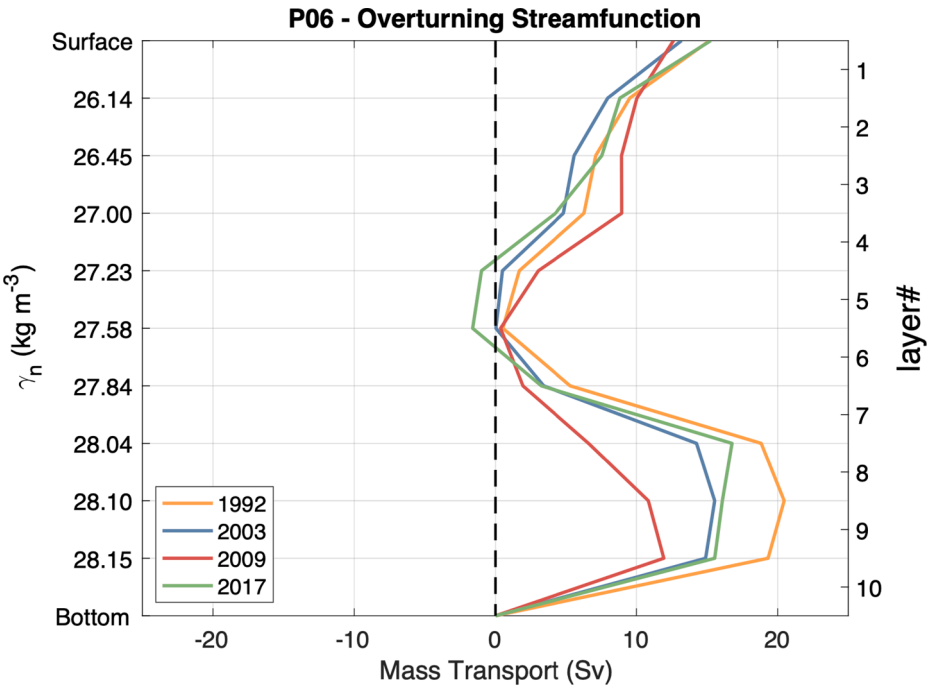

Fig. 7. Overturning mass transport stream function across 32°S in the Pacific Ocean for 1992, 2003, 2009 and 2017. This function is computed as the zonally- and vertically-integrated mass transports in isoneutral layers (along the entire section and from the seafloor to the sea surface).

Table 3
Intensity of the deep Pacific Meridional Overturning Circulation (PMOC) results for the Pacific Ocean (P06) at 32°S in 1992, 2003, 2009 and in 2017. Negative (southward) deep transports are summed to estimate the PMOC.

Year	PMOC (Sv)
1992	−19.9 ± 7.4
2003	−15.5 ± 7.9
2009	−11.6 ± 8.0
2017	−18.4 ± 6.5

2003, 2008) that can be also observed in our results for 1992, but not in 2017. The intensity of the overturning, called Pacific Meridional Overturning Circulation (PMOC), is generally described as the maximum in the overturning streamfunction, comprising equatorward flow within the South Pacific Ocean and returning poleward flow as PDW (1500–4000 m). The PMOC in 1992 and in 2017 shows the same pattern as in 2003 and in 2009. However, as shown in Table 3, the PMOC presents a minimum in 2009 (−11.6 ± 8.0 Sv), although not significantly different from the PMOC in 1992 (−19.9 ± 7.4 Sv), 2003 (−15.5 ± 7.9 Sv) and 2017 (−18.4 ± 6.5 Sv).

6. Horizontal distribution of final adjusted transport

Fig. 8 shows the eastward zonally accumulated mass transport in isoneutral layers for 1992 and 2017, and for 2003 and 2009 computed by Hernández-Guerra and Talley (2016). The accumulated transport is obtained by integrating the mass transport in each layer eastward from zero at the western boundary, and then summing together northward and southward layer transports as in Fig. 6. The Pacific Ocean is then divided into a three-layer system: northward mass transport in the uppermost layers (1–5, Fig. 8a), southward in the deep layers (6–8, Fig. 8b), and northward in the abyssal layers (9–10, Fig. 8c).

6.1. Upper ocean circulation

The accumulated upper ocean mass transport (Fig. 8a), consisting of thermocline and intermediate waters (surface to $\gamma^n = 27.58$ kg/m^3, about 1500 m depth), presents an intense western boundary current flowing poleward, an equatorward recirculation east and close to the western boundary, and a net equatorward Sverdrup mass transport across the ocean interior with a wide and slow Peru-Chile Current in the eastern boundary, representing the usual subtropical gyre feature. Eddies are responsible for the alternating mass transports present along the whole subtropical gyre and are intensified in the westernmost part of the circulation, corresponding to the Tasman Sea as noted in both Hernández-Guerra and Talley (2016) and Wijffels et al. (2001).

6.1.1. Interior gyre circulation

The Pacific Ocean interior circulation for 1992, 2003 and 2017 differs noticeably from that of 2009 (Fig. 8a). These marked differences are also found in deep and bottom accumulated mass transports (Fig. 8b and c). West of the TKR, located at approximately 175°W encompassing the Tasman Sea and South Fiji Basin, the horizontal mass transports for the three years are similar, with net poleward mass transport dominated by the southward EAC and its equatorward recirculation, and a major eddy field. The ocean circulation of the full water column across the mid-Pacific, between the TKR and the East Pacific Rise (EPR) at 110°W, is significantly different in 2009 compared with the ocean circulation in 1992, 2003 and 2017.

In the upper layers, the 2003 mass transport is a “classic gyre” with a northward mass transport from the TKR to the EPR, whereas in 2009 the structure of the mass transport is a “bowed gyre”, reaching maximum southward values at around 140°W, then rebounding with compensating equatorward mass transport (Hernández-Guerra and Talley, 2016). The pattern of the circulation in 2017 has changed from the “bowed” circulation in 2009, and resembles again the “classic gyre” of 1992 and 2003. The mass transports for the four years seem to coalesce at the EPR, with a net equatorward mass transports of 14.7 ± 2.5 Sv in 1992, 13.2 ± 2.2 Sv in 2003, 12.3 ± 2.3 Sv in 2009 and 16.9 ± 2.4 Sv in 2017. Therefore, the net northward mass transports obtained in 1992 and in 2017 are comparable with the estimated mass transports previously computed by Ganachaud (2003) for 1992 (16.1 ± 5.1 Sv), and for 2003 and 2009 computed by Hernández-Guerra and Talley (2016). The “bowed gyre”, subject to significant interannual variability (McCarthy

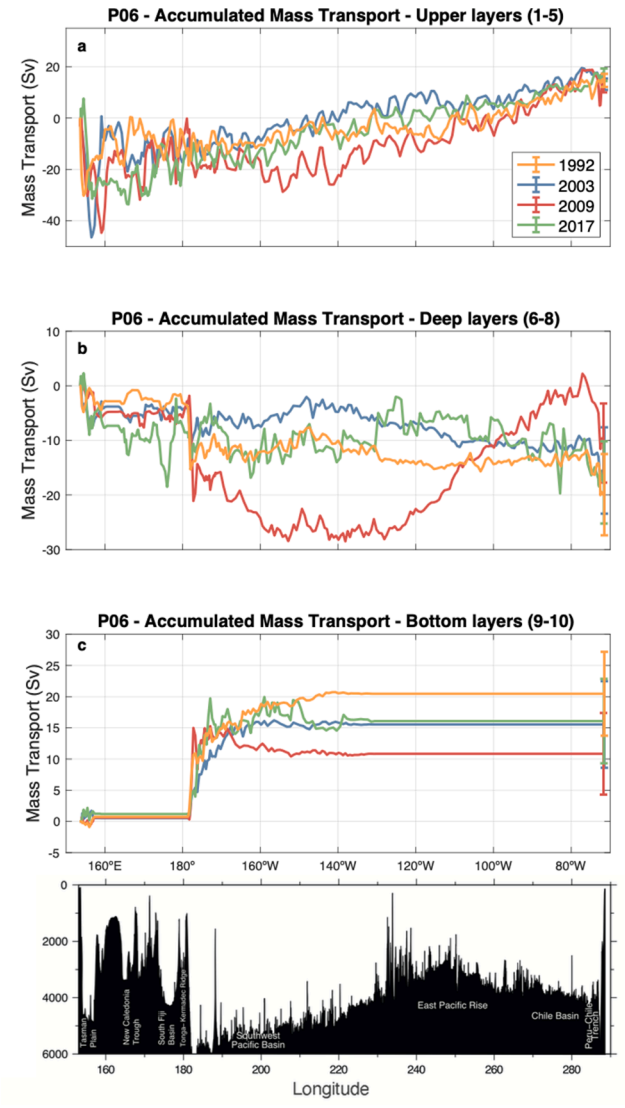

Fig. 8. Eastward accumulated mass transport (Sv) at 32°S in the Pacific Ocean for (a) upper, (b) deep, and (c) bottom layers for 1992, 2003, 2009 and 2017. Bottom plot shows the bathymetry for reference.

et al., 2000), was previously observed by Wyrtki (1975) with a classic surface dynamic model, and by McCarthy et al. (2000). Using the original WOCE P06 section in 1992, Wijffels et al. (2001) identified a double gyre. In contrast, Reid (1997)'s surface circulation showed a circulation similar to the "regular gyre" years as in our results.

6.1.2. *Western boundary current: East Australian Current (EAC)*

The EAC is an intense western boundary current that flows southward offshore along the east Australian continental boundary. Recent studies at approximately 32°S indicate that most of the EAC poleward mass transport is confined between the continental shelf to ~ 155°E, a width of approximately 123 km, with a relative intense net northward return flow to the east of the boundary current (Chiswell et al., 1997; Hernández-Guerra and Talley, 2016; Ridgway and Godfrey, 1994; Talley et al., 2011). From the hydrographic sections analyzed in this study, the EAC has a width from approximately 79 km in 1992 to 517 km in 2009, which covers the approximately 123 km estimated by Sloyan et al. (2016) from 18-month mean along-slope velocity. As seen in Fig. 9, the EAC includes both upper and deep layers (Layers 1–8) and presents a net poleward mass transport of −35.1 ± 2.0 Sv in 1992 and of −39.2 ± 1.6 Sv in 2017 (Table 4 and Fig. 8). The maximum southward mass transport is found at 156.6°E in 2017, which is close to the 2003 estimate by Hernández-Guerra and Talley (2016), and the minimum position is found at 154.5°E in 1992. The offshore equatorward recirculation of the EAC, extending approximately 2° eastward from the EAC, is summed over both upper and deep layers (Layers 1–8), and this recirculation presents a mass transport weaker than the EAC in 1992 (17.2 ± 1.9 Sv from 154.3° to 156.7°E), and in 2017 (12.3 ± 2.5 Sv, between 156.6° and 158.5°E).

EAC mass transports for 1992 and 2017, according to the results shown in this study, are comparable to the previous estimates for the 1992 WOCE P06 section: −40 ± 8 Sv reported by Macdonald et al. (2009), and −36 ± 10 Sv reported by Ganachaud and Wunsch (2003). However, Wijffels et al. (2001) reported a much weaker EAC mass transport for the early 1990 s of −22.1 ± 4.6 Sv, with a rms variability of 32 Sv estimated from altimetry, based on their 1991–1994 current meter study accompanied by ten EAC hydrographic sections from the coast of Australia to 154.4°E (Mata et al., 2000). Most recently, Hernández-Guerra and Talley (2016) estimated a stronger EAC mass transport of −51.1 ± 2.0 Sv and −49.9 ± 2.1 Sv for 2003 and 2009, respectively, based on the mass transports for the whole water column. Since Fig. 9 suggests that the EAC mass transport is present only in layers 1–8, the resulting mass transports of this current are recalculated for these layers obtaining a poleward mass transport of −54.3 ± 2.6 Sv and of −50.5 ± 2.0 Sv in 2003 and 2009, respectively. These results are not significantly different from those estimated by Hernández-Guerra and Talley (2016) and are listed in Table 4. EAC recirculation presents a relatively intense net northward mass transport adjacent to the EAC, flowing over both upper and deep waters in the South Pacific Ocean (Fig. 8 and Table 4). The offshore equatorward recirculation of the EAC presents a mass transport weaker than the EAC in 2009 (30.4 ± 1.6 Sv, between 158.9° and 160.8°E) as in 1992 and 2017 (Table 4). However, in 2003 the equatorward EAC recirculation, from 156.3° to 158.9°E, has a similar mass transport (52.1 ± 4.2 Sv) to the poleward EAC transport (Table 4). These results are consistent with time series of a full-depth current meter and property mooring array at 27°S analyzed by Sloyan et al. (2016): their results showed a weaker EAC recirculation in most occasions, but also a stronger than or of similar magnitude to that of the southward EAC transport in different periods.

Under a changing climate, the EAC has been found to be strengthening over the last decades (Johnson et al., 2011; Wu et al., 2012). However, our results show that the EAC increased in mass transport from 1992 (−35.1 ± 2.0 Sv) to 2003 (−54.3 ± 2.6 Sv), and then decreased slightly in mass transport in 2009 (−50.5 ± 2.0 Sv) and 2017 (−39.2 ± 1.6 Sv), with a very vigorous eddy field across the topographically-complex Tasman Sea, between the Australian coast and the Tonga-Kermadec Ridge (Table 4). This fact could be explained by seasonal variability, as the EAC presents a stronger poleward flow in summer (Oke et al., 2019; Ridgway, 2007), with a seasonal amplitude up to 6.2 Sv (Archer, et al., 2017; Kerry and Roughan, 2020; Ribbat, et al., 2020; Ridgway and Godfrey, 1997). This behavior is observed in our results: the EAC presents stronger transport in 2009, which section was in November (summer), than in July (winter) in 1992 and 2017, except in 2003 that presents a similar value possibly due to interannual variability.

6.1.3. *Eastern boundary current: Peru-Chile Current (PCC) and Peru-Chile Undercurrent (PCUC)*

The PCC is the eastern boundary current in the Pacific Ocean. As any other eastern boundary current, like the Canary Current in the North Atlantic Subtropical Gyre (Casanova-Masjoan et al., 2020; Hernández-Guerra et al., 2017; Vélez-Belchí et al., 2017), it is difficult to identify in the accumulated mass transport due to the fact that the current is weak (~3–4 Sv estimated by Shaffer et al. (2004)) and the variability induced by the eddy field is relatively strong.

The equatorward PCC is evident in the upward slope of the isotherms and isoneutrals in the upper layers (>700 m) off the west coast of South

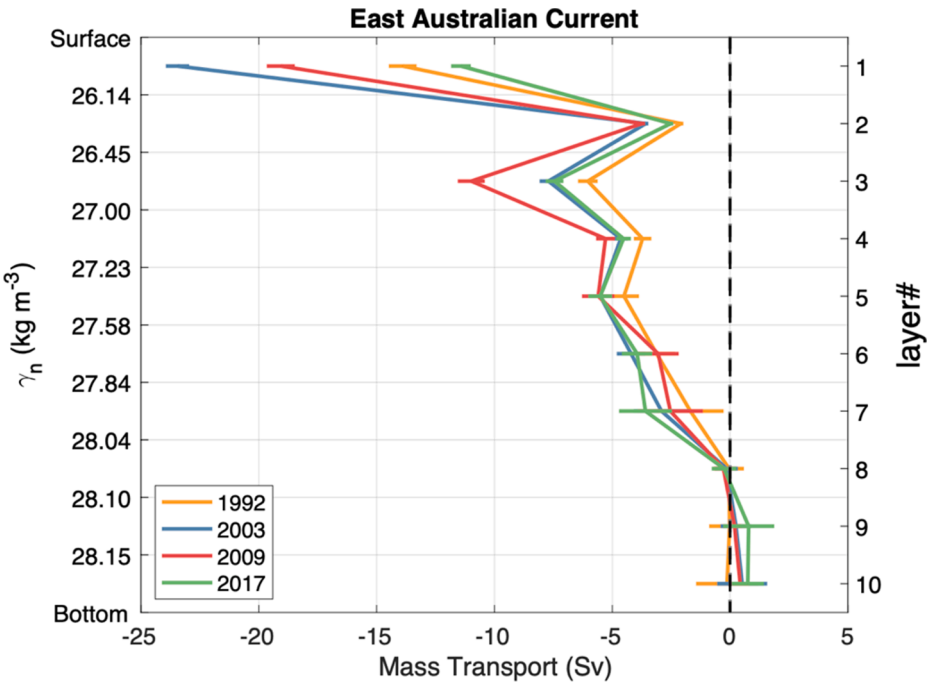

Fig. 9. Mass transport (Sv) per layer corresponding to the East Australian Current at 32°S in the Pacific Ocean for 1992, 2003, 2009 and 2017.

Table 4
Mass transports inverse model results and uncertainty (Sv) for the East Australian Current, East Australian Current recirculation, Peru-Chile Current, Peru-Chile Undercurrent and Deep Eastern Boundary Current for the Pacific Ocean (P06) at 32°S in 1992, 2003, 2009 and 2017. Positive transports are northward and negative transports are southward.

Mass Transport (Sv)	Longitude	Layers	Final 1992	Final 2003	Final 2009	Final 2017
East Australian Current	Coast to 154.3°E (1992) Coast to 156.3°E (2003) Coast to 158.9°E (2009) Coast to 156.6°E (2017)	1:8	−35.1 ± 2.0	−54.3 ± 2.6	−50.5 ± 2.0	−39.2 ± 1.6
East Australian Current Recirculation	154.3° to 156.7°E (1992) 156.3° to 158.9°E (2003) 158.9° to 160.8°E (2009) 156.6° to 158.5°E (2017)	1:8	17.2 ± 1.9	52.1 ± 4.2	30.4 ± 1.6	12.3 ± 2.5
Peru-Chile Current	85°W to coast	1:3	4.4 ± 1.0	3.3 ± 0.9[a]	2.3 ± 0.8[a]	4.4 ± 0.8
Peru-Chile Undercurrent	75°W to coast	4:5	–	−2.8 ± 1.2[a]	−3.8 ± 1.2[a]	−1.5 ± 0.8
Deep Eastern Boundary Current	76.3°W to coast (1992) 78.6°W to coast (2003) 78.8°W to coast (2009) 86.0°W to coast (2017)	6:7	−6.9 ± 4.9	−5.3 ± 5.5	−9.3 ± 5.0	−8.5 ± 6.8

[a] Final mass transports computed by Hernández-Guerra and Talley (2016).

America (Fig. 2) (Strub et al., 1998; Talley et al., 2011; Tsimplis et al., 1998). The Peru-Chile Undercurrent (PCUC) is found below the PCC (Wooster and Reid, 1963), and extends over the continental shelf and slope, where the isotherms and isoneutral slope downward (Shaffer et al., 1999). Following Hernández-Guerra and Talley (2016), the PCC is estimated from the surface toγ^n = 27.0 kg/m^3 (Layers 1–3) and from 85°W to the coast of Chile, while the PCUC in the Layers 4–5 and from 75°W to the Chilean coast (Table 4). Thus, the flow of PCC is estimated to be 4.4 ± 1.0 Sv in 1992, 3.3 ± 0.9 Sv in 2003, 2.3 ± 0.8 Sv in 2009, and 4.4 ± 0.8 Sv in 2017, which are all not significantly different, except for 2009. The PCUC does not appear in 1992, and the mass transport is estimated to be −2.8 ± 1.2 Sv in 2003, −3.8 ± 1.2 Sv in 2009, and of −1.5 ± 0.8 Sv in 2017, which again shows that the estimations for 2003 and 2017 are not significantly different, but that a more intense PCUC is found in 2009. These results are consistent with the moderate average estimated mass transport of the PCUC at 30°S of 1–1.3 Sv previously reported by Huyer et al. (1987), Shaffer et al. (2004), and Shaffer et al. (1999). According to the Sverdrup relation (Sverdrup, 1947), a negative nearshore wind stress curl (WSC) drives a poleward mass transport. According to Vergara et al. (2016), the poleward decrease of WSC in 2009 could be related to the poleward increase in the PCUC intensity of that year. Interestingly, Chaigneau et al. (2013) estimated a strong PCUC intensification in winter 2010 using SADCP data, similar to the intensification estimated in our results for the P06 cruise in 2009 that took place in the eastern boundary in winter 2010.

6.2. Deep ocean circulation

Fig. 8b shows the accumulated mass transport for the PDW layers (layers 6–8). The net poleward mass transport of PDW through 32°S in 1992 (−19.9 ± 7.4 Sv), 2003 (−15.5 ± 7.9 Sv), 2009 (−10.5 ± 7.3 Sv), and in 2017 (−17.7 ± 7.5 Sv) are not significantly different. The overall zonal structure for 1992 and 2017 is remarkably different from 2009, but similar to 2003. There are two deep western boundaries, one at ~ 155°E and the other one at ~ 175°W. The mass transport at ~ 155°E, which corresponds to the deepest part of the EAC as shown in Mata et al.

(2000), does not present any significant difference in 1992 (−3.3 ± 2.5 Sv), 2003 (−5.3 ± 3.7 Sv), 2009 (−5.4 ± 1.9 Sv) and 2017 (−6.4 ± 2.0 Sv). In contrast, noticeable differences are shown in the mass transport at approximately 175°W, with a southward mass transport of −10.7 ± 2.6 Sv in 1992, −5.3 ± 3.7 Sv in 2003, the strongest southward mass transport in 2009 (−17.9 ± 4.0 Sv), and −4.0 ± 6.0 Sv in 2017. In 1992, 2003 and 2017 -the "classic gyre" years- net poleward mass transport was mostly accomplished by gradual accumulation of mass transport across the width of the section. In 2009, the "bowed gyre" year, the large southward mass transport in the Southwest Pacific Basin, obtained between the deep western boundary found at 175°E and west of 140°W, is compensated by northward flow across eastern Pacific to about 78°W (of about 25 Sv), and then a southward flow in the eastern boundary, with a net mass transport similar to the other years (Hernández-Guerra and Talley, 2016).

Furthermore, a narrow deep eastern boundary current in the Chilean basin, previously described by Schulze Chretien and Speer (2019) and Shaffer et al. (2004), is centered above the Peru-Chile Trench at about 2500–3400 m depth (Layers 6–7) and from ~ 85°W to the Chilean coast. This current presents a poleward mass transport of −6.9 ± 4.9 Sv in 1992, −5.3 ± 5.5 Sv in 2003, −9.3 ± 5.0 Sv in 2009, and −8.5 ± 6.8 Sv in 2017 (Table 4). The southward mass transports of this boundary current are consistent with the approximately −5 Sv in all four occupations previously estimated using WOCE P06 data by Shaffer et al. (2004) for 1992, and by Schulze Chretien and Speer (2019) for the 2003, 2009, and 2017.

6.3. Abyssal ocean circulation

Fig. 8c presents the accumulated mass transport for the LCDW layers. The mass transport for layers 9 and 10, as shown in Fig. 6a, describes a northward flow into the Pacific close to the TKR to 140°W (Fig. 8c). The net abyssal northward mass transport in 1992 (20.5 ± 6.7 Sv), 2003 (15.5 ± 6.9 Sv), 2009 (10.8 ± 6.5 Sv), and in 2017 (16.1 ± 6.8 Sv) are not significantly different. In 1992, 2003 and 2017, the equatorward mass transport was broadly distributed over the deepest part of the Southwest Pacific Basin. However, most of the northward mass transport in 2009 is in the narrow DWBC, which resembles Reid (1997)'s abyssal circulation maps based on a 1968 hydrographic section.

7. Numerical ocean models

Ocean models give a description of the state of the ocean's evolution over time. From these models, data covering the period of each hydrographic section have been used (Figs. 10 and 11), with the aim of identifying whether the observed changes in circulation are reproduced

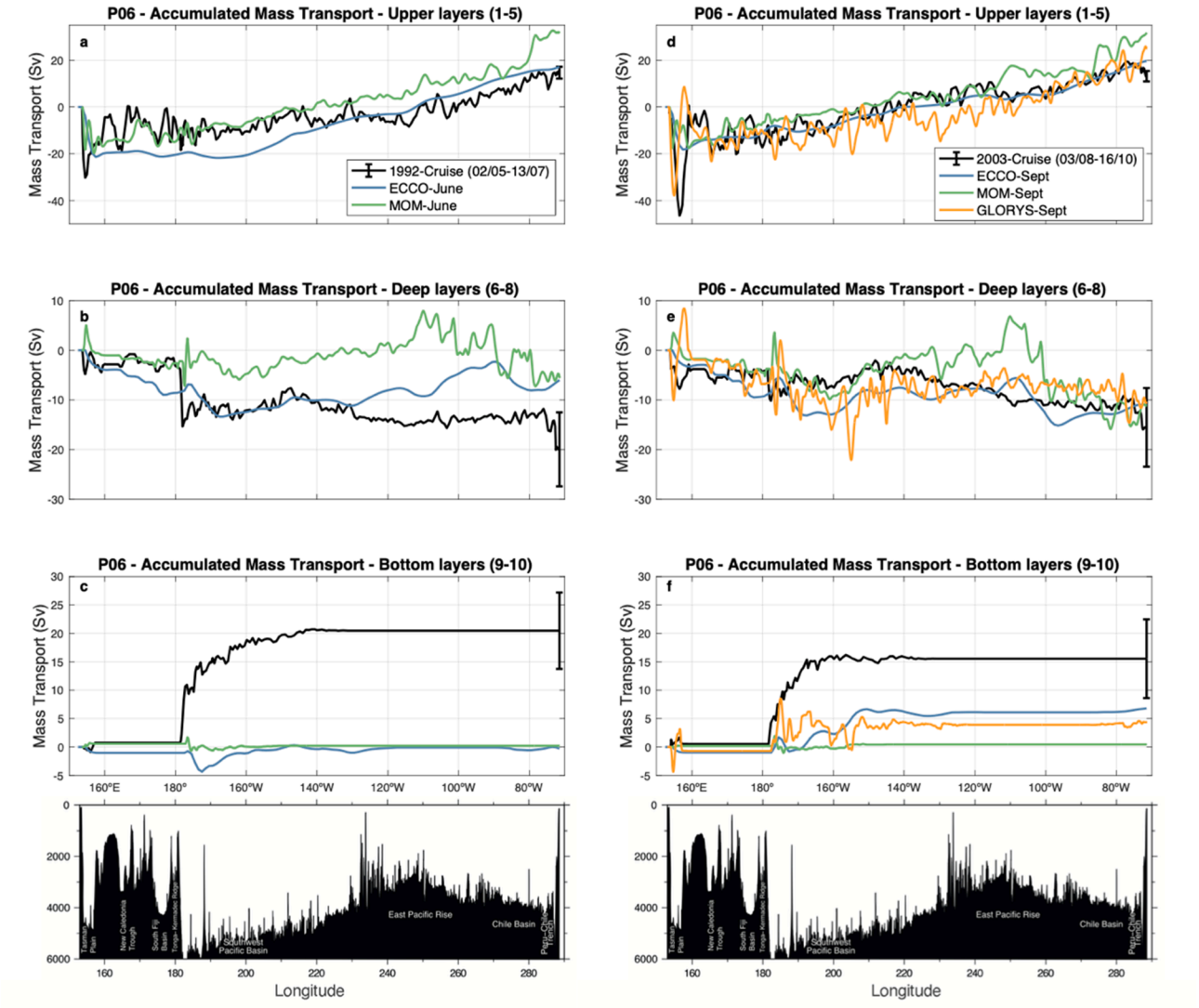

Fig. 10. Eastward accumulated mass transport (Sv) at 32°S in the Pacific Ocean for (a, d) upper, (b, e) deep, and (c, f) bottom layers for 1992 and 2003, respectively, estimated from hydrographic data and from the ocean models ECCO, GLORYS, and MOM.

by these models and to try to find out whether the 2009 "bowed gyre" circulation has occurred in other periods.

The model outputs (ECCO, SOSE, GLORYS, and MOM) show roughly similar patterns as the hydrographic data in the upper layers for 1992, 2003, 2009 and 2017 (Fig. 10a, 10d, 11a, and 11d) although, as previously mentioned, with a weaker EAC and a similar pattern circulation in in the ocean interior for the upper layers. In the deep layers (Fig. 10b, 10e, 11b, and 11e), none of the models is able to represent the strong poleward mass transport east of TKR, possibly due to their relatively coarse horizontal resolution. In fact, only the eddy-resolving GLORYS reanalysis shows a distinct poleward transport intensification in 2009. In contrast, models show a roughly similar pattern in circulation as hydrographic data in the ocean interior except in 2009. In abyssal layers, models noticeably differ from the hydrographic data in 1992, 2003, and 2017 (Fig. 10c, 10f, and 11f), with very weak LCDW equatorward transports. Interestingly, all models simulate transports close to the hydrographic data, both in terms of zonal structures and accumulated transports, in the bottom layers of 2009 (Fig. 11c). Finally, none of the ocean models reproduces the "bowed" circulation of the hydrographic data present in 2009.

8. Rossby wave dynamics as responsible for circulation variability

Large-scale Sea Surface Height Anomalies (SSHA) at 30°S in the South Pacific Ocean are investigated using satellite altimetry data from the AVISO product for the past 27 years (http://las.aviso.oceanobs.com), which are instrumental in clarifying the dynamics underlying mesoscale eddies and Rossby waves. Fig. 12 presents two Hovmöller diagrams of the SSHA along 30°S from January 1993 to December 2019. Fig. 12a and 12b are obtained after removing the trend and the steric component following Chelton and Schlax (1996). In Fig. 12b, a low-pass filter is also applied to the SSHA observations to retain scales longer than 110 days and larger than 7° of longitude.

This diagram shows large-scale, westward propagating disturbances of 10–15 cm amplitude as also noted in Hernández-Guerra and Talley (2016). These disturbances are initiated in the eastern Pacific, at ~ 100°W, similar to the previously described ~ 100°–120°W region by Hill et al. (2010) and Li et al (2020). This region is close to the EPR where topographic steering over the ridge topography produces an intensification of the baroclinic Rossby wave signals produced by a WSC perturbation in the central South Pacific. These waves are intensified as they propagate westward, taking approximately 5–7 years to cross the 8500 km to NZ, which corresponds to a speed of 3 cm/s. This is

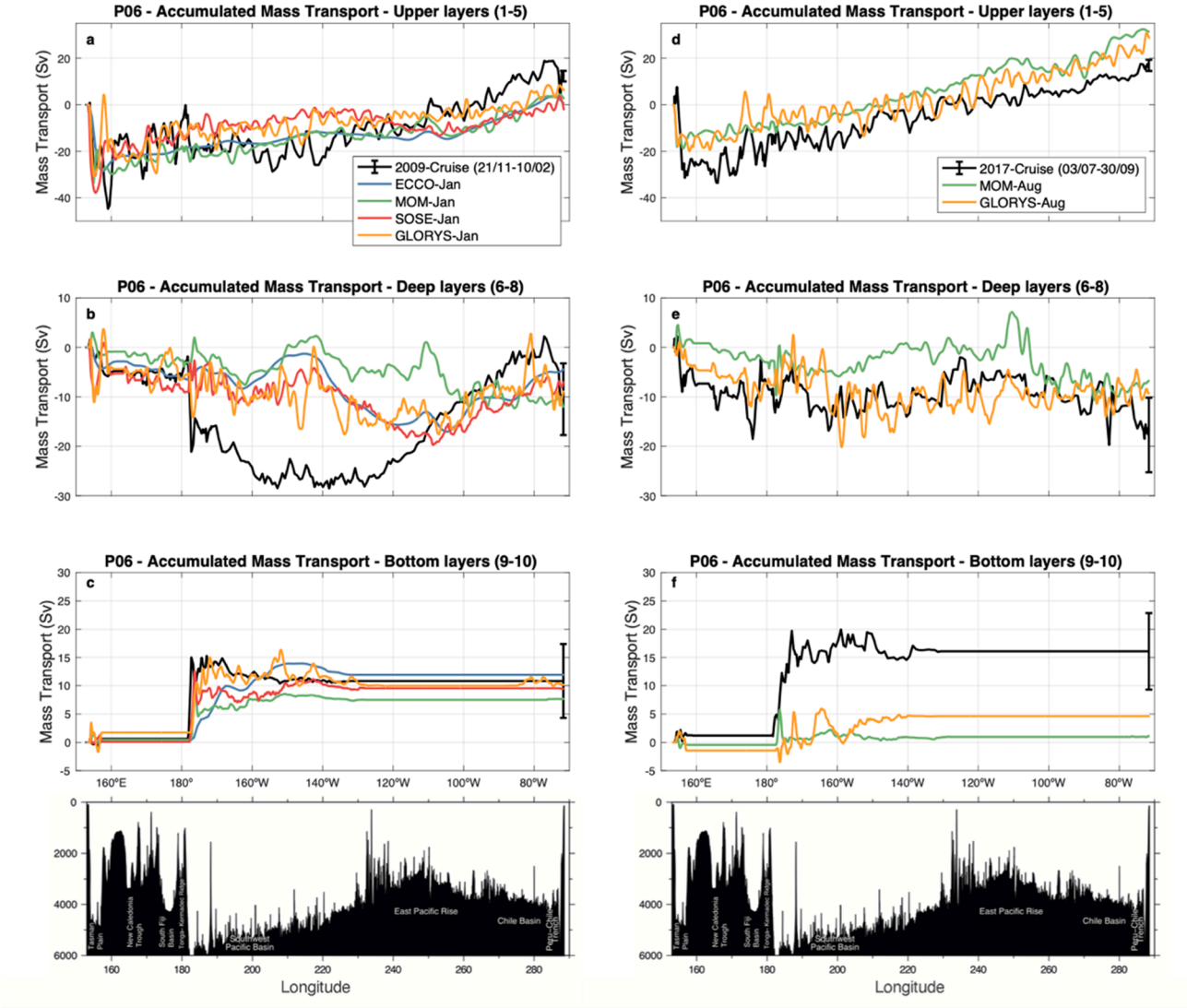

Fig. 11. Eastward accumulated mass transport (Sv) at 32°S in the Pacific Ocean for (a, d) upper, (b, e) deep, and (c, f) bottom layers for 2009 and 2017, respectively, estimated from hydrographic data and from the ocean models ECCO, SOSE, GLORYS, and MOM.

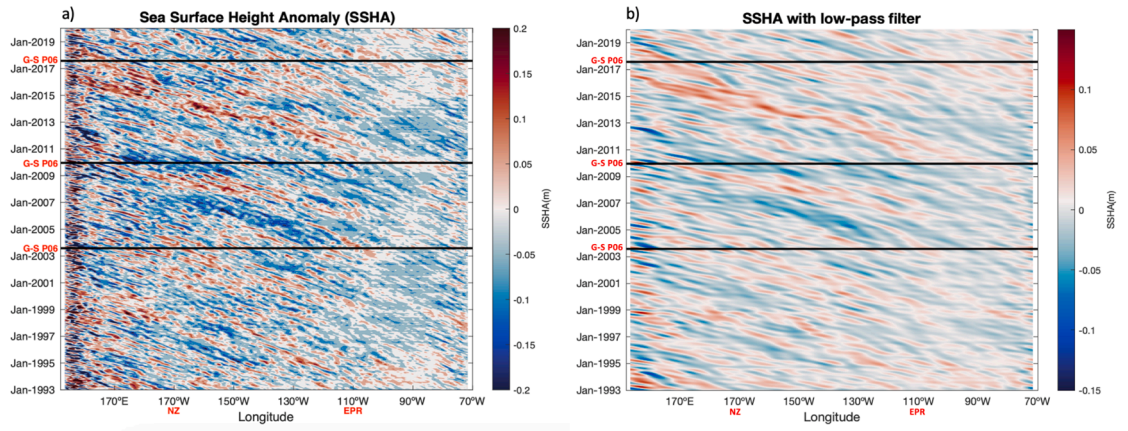

Fig. 12. Sea Surface Height Anomaly (m) along 30°S in the Pacific Ocean for the altimetry complete time series from January 1993 to December 2019. The trend and the steric component are removed to a) and b); and a low-pass filter is applied to retain scales longer than 110 days and larger than 7° of longitude to b). The GO-SHIP (G-S) P06 cruise periods in 2003, 2009, and 2017 are indicated. The longitudes of New Zealand (NZ) and East Pacific Rise (EPR) are also shown. Merged AVISO product (http://las.aviso.oceanobs.com).

approximately the speed of long baroclinic Rossby waves at this latitude. The corresponding westward intensification was previously reported by Moore and Wilkin (1998) using results from the Los Alamos National Laboratory global ocean model, which properly represents planetary long waves. In addition, using different Pacific current meter arrays, they described a persistent train of crests and troughs west of 175°W, approximately along the TKR, where most of the long-wave energy is lost into an eastward topographic wave. As indicated in Hernández-Guerra and Talley (2016), the 2003 P06 section was occupied when an anomalously lower SSHA was centered over the EPR and a high SSHA over the southwest South Pacific Basin. A downwelling Rossby wave was present in the central Pacific between 160°W and 150°W when the 2009 P06 occurred. Finally, the 2017 P06 occurred during a period with alternate high and low SSHA over the Southwest Pacific Basin.

8.1. Linear Rossby wave model

To study the causes of the observed spatially varying SSHA signals in 2009, as visualized in Fig. 12, a linear Rossby wave model is adopted following Fu and Qiu (2002) and Vélez-Belchí et al. (2017). The model includes the WSC variability, and the responses forced by SSHA changes along 28 − 32°S. The long-wave equation for the sea surface height, h, is

$$\frac{\partial h}{\partial t} - \frac{\beta g^{'} H_e}{f^2}\frac{\partial h}{\partial x} = -\frac{g^{'} H_e^2 \nabla \times \tau}{\rho_0 g f H_1^2} \quad (1)$$

where t is time, x is the longitudinal coordinate (positive eastward), H_e is the equivalent depth of the model ($H_e = H_1 H_2/(H_1 + H_2)$), H_1 and H_2 are the upper- and lower-layer thicknesses respectively, ρ_0 is the mean density of sea water, $g^{'} = \left(\frac{\delta\rho}{\rho_0}\right) g$ is the reduced gravity ($\delta\rho$ is the density difference between the two layers), f is the Coriolis parameter, and β is its meridional gradient. Integrating Eq. (1) along the Rossby wave characteristics in the x-t plane we obtain the following solution:

$$h(x,t) = h\left(x_e, t - \frac{x - x_e}{c}\right) - \frac{f H_e}{\rho_0 g \beta H_1^2}\int_{x_e}^{x} \nabla \times \tau\left(x^{'}, t - \frac{x - x^{'}}{c}\right) \quad (2)$$

where $c = -\frac{\beta g^{'} H_e}{f^2}$ is the phase speed of long baroclinic Rossby waves, x_e is the longitudinal location of the eastern boundary. The first and second term in the RHS of Eq. (2) represent the influence of the free Rossby waves propagating from the eastern boundary and the effects of wind forcing, respectively.

Eqs. (1) and (2) can be solved from zero initial conditions in a forward time-stepping mode using the WSC anomaly across 30°S obtained from the reanalysis wind products of NCEP that were used in the inverse modeling. Following Fu and Qiu (2002), we set g'= 0.03 m/s^2, H_1 = 440 m and $H_1 + H_2$ = 5000 m, leading to H_e = 400 m.

Fig. 13a presents the results of SSH difference between the eastern boundary and the western boundary (from 175°E to 68°W) for the upper layers due to baroclinic waves. As shown in Fig. 8, the net equatorward mass transports of the four hydrographic sections are not significantly different in the upper layers. Thus, as the linear wave model has used the same upper layers, the differences in SSH shown in Fig. 13a are expected to match during the four sections. This is true for 2003 (23.4 ± 0.1 cm), 2009 (23.7 ± 0.3 cm) and 2017 (24.7 ± 0.3 cm), but it is not the case for 1992 (22.5 ± 0.2 cm), which is characterized by a relatively weak SSH difference, possibly suggesting that wind stress data during this year were not appropriate.

The difference in SSH between 140°W and 68°W, presented in Fig. 13b, corresponds to the slope of the sea surface at each time. A large positive slope of the sea surface indicates a strong mass transport flowing north and, therefore, a weaker net southward mass transport. Conversely, if the positive slope is weakened, the flow due to Rossby waves would still be directed northwards but with less intensity, thus resulting in a weaker northward mass transport and a larger net southward mass transport. Fig. 13b shows a weaker slope in 2009 (14.7 ± 0.1 cm) than in 2003 (16.6 ± 0.1 cm) and 2017 (16.5 ± 0.2 cm). Consequently, the poleward mass transport between 140°W and 68°W in 2009 had to be the highest, as corroborated in Fig. 8. Again, the results for 1992 (14.6 ± 0.2 cm) suggest that the wind data during this year were not appropriate, as they disagree with the hydrographic data circulation pattern. It is worth mentioning that this model suggests another "bowed gyre" event in the period of 2000–2002 (<14 cm), that can presumably be observed in the low SSHA during this period in Fig. 12.

Fig. 14 presents four Hovmöller diagrams of the SSHA along 30°S obtained using output of numerical modelling data. In the output of ECCO and SOSE (Fig. 14a and 14b), the Rossby wave originated at 110°W is not present in 2005, however, we can see the low SSHA found at ~ 175°W in 2009 but not its propagation. Fig. 14d shows the SSHA using the MOM output, where the Rossby wave originated at 110°W in 2005 with negative SSHA cannot be observed, as well as the low SSHA found at ~ 175°W in 2009.

In contrast, Fig. 14c shows that the Hovmöller diagram obtained with the output of the GLORYS model is very similar to the in situ data (Fig. 12). To find out why the GLORYS model shows the Rossby wave signal in the Hovmöller diagram but not the "bowed gyre" circulation in the accumulated mass transport in 2009, Fig. 15 presents transpacific

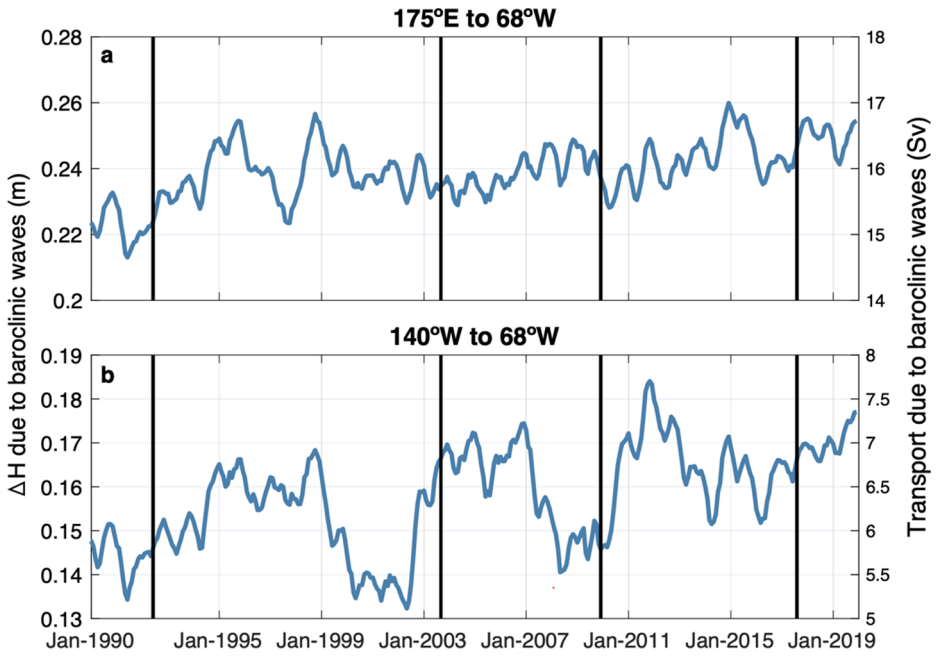

Fig. 13. Sea surface height difference (m) at 28-32°S and its corresponding transport (Sv) in the Pacific Ocean from the Rossby wave model, obtained using the NCEP wind stress curl from (a) 175°E to 68°W and from (b) 140°W to 68°W. Black vertical lines mark the times of the cruises.

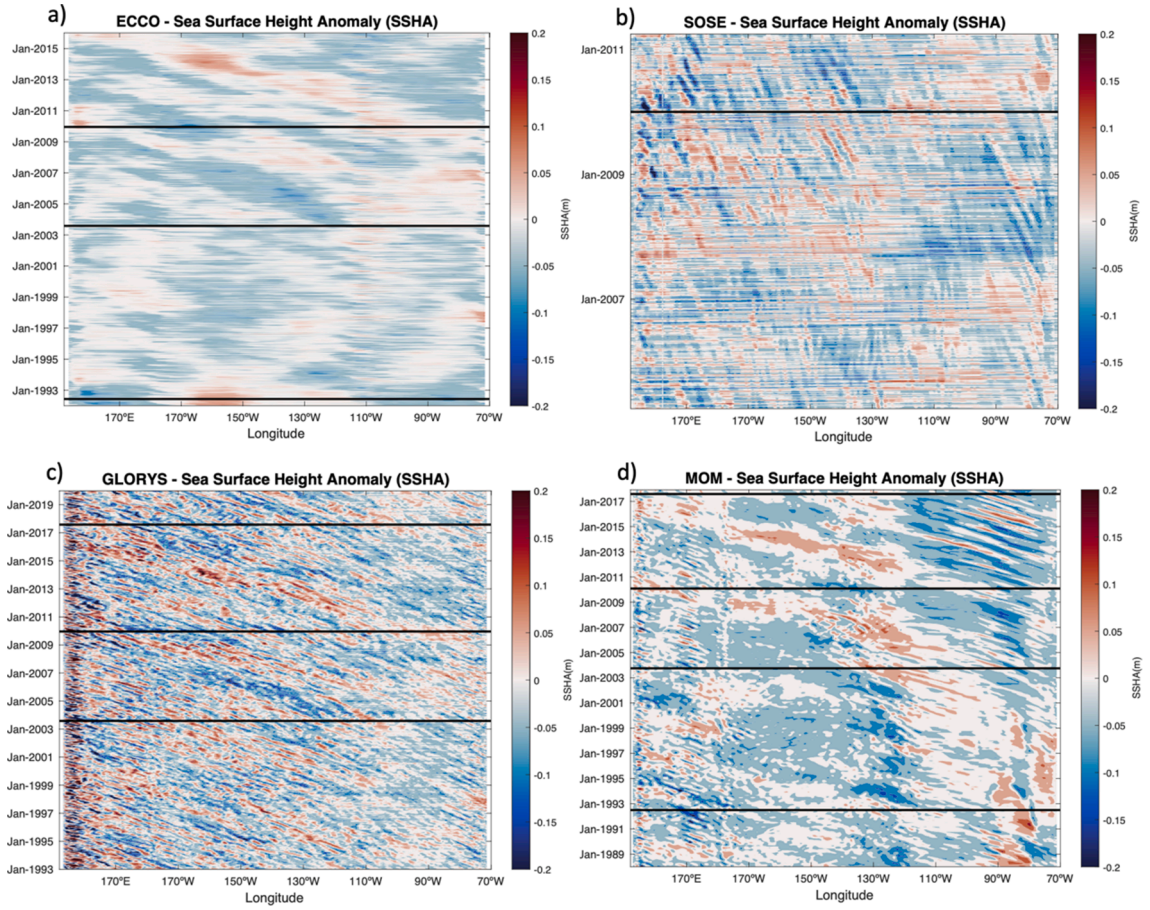

Fig. 14. Sea Surface Height Anomaly (m) along 30°S in the Pacific Ocean for the altimetry time series of (a) ECCO, (b) SOSE, (c) GLORYS, and (d) MOM.

vertical sections of potential temperature (a) and salinity (b) differences between GLORYS and hydrographic data in 2009, which indicate that the vertical stratification of potential temperature and salinity data at the thermocline layer of both data set are different. The panel (a) shows warm bias and (b) shows high-salinity bias of the GLORYS model. In terms of geostrophic transport, the dynamic height has a high-bias from

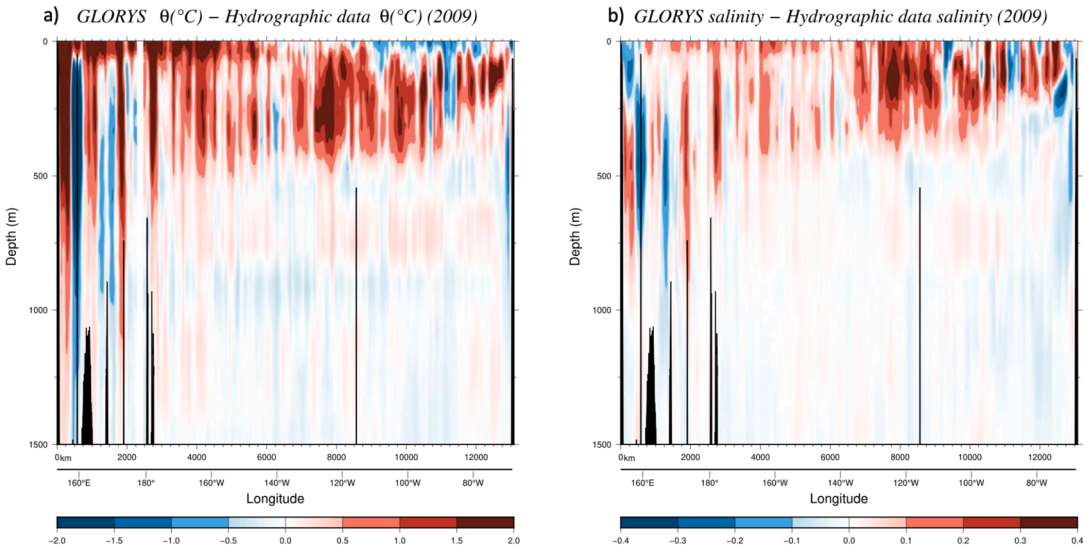

Fig. 15. Vertical sections for the GLORYS data and hydrographic data differences of (a) potential temperature (°C) and (b) salinity along section P06 in the Pacific Ocean.

temperature and a low-bias from salinity. Indeed, at a potential temperature of 10 °C, salinity of 34.8 psu, and pressure of 300 dbar, the thermal expansion is about $1.7 \cdot 10^{-4}$ and the haline contraction is about $7.5 \cdot 10^{-4}$. Moreover, Fig. 10 shows the warm bias is roughly 1 °C and high-salinity bias is about 0.2 psu. While salinity bias is 1/5 in magnitude of the potential temperature bias, haline contraction is about 4 times larger and thus thermal and haline effects are compensating. This compensation is much weaker west of 140°W where high-salinity bias is suppressed. There, the warm bias gives a density anomaly of $1.7 \cdot 10^{-4}$ *1 (°C) * 1025 (kg/m^3) = 0.17 kg/m^3 density anomaly over a 400 m tall water column, which translates into $400 \cdot 10^4$ (depth [Pa]) * (1/(1025–0.17) − 1/1025 [kg/m^3]) / 9.8 (gravity [m/s^2]) = 6.6 cm dynamic height anomaly. Therefore, GLORYS model simulates the low SSH anomaly in 2009, but this low dynamic height anomaly is compensated by the high dynamic height anomaly in the upper 400 m caused by warm anomaly in the GLORYS and its failure to reproduce the internal pressure field correctly. Consequently, GLORYS model does not reproduce the 'bowed' circulation.

9. Temperature and freshwater transports

Table 5 shows a comparison between the temperature transport (in PW) and freshwater flux (in FSv, Sverdrup for freshwater transport without mass balance) for the section P06 in 1992 and in 2017 resulting from this work and those estimated by Hernández-Guerra and Talley (2016) for 2003 and 2009.

Meridional temperature transports from the inverse model in 1992 (0.42 ± 0.12 PW), 2003 (0.38 ± 0.12 PW), 2009 (0.16 ± 0.12 PW), and 2017 (0.42 ± 0.12 PW) indicate that the results are all not significantly different except for the temperature transport estimated in 2009 (Table 5).

Table 5
Temperature transport (PW) and net freshwater transport (FSv), which is equivalent to the net evaporation minus precipitation (positive is net evaporation), for the Pacific Ocean north of 32°S.

Year	Temperature Transport (PW)	Freshwater Flux (FSv)
1992	0.42 ± 0.12	0.26 ± 0.08
2003[a]	0.38 ± 0.12	0.25 ± 0.02
2009[a]	0.16 ± 0.12	0.50 ± 0.03
2017	0.42 ± 0.12	0.34 ± 0.08

[a] Heat transports and freshwater fluxes computed by Hernández-Guerra and Talley (2016).

The freshwater flux is estimated following Joyce et al. (2001):

$$\overline{F} = \sum_i \sum_j T_{ij} S'_{ij} / S_0$$

where T_{ij} is the absolute mass transport, S'_{ij} is the anomaly of salinity (Salinity-S_0), both in layer i at station pair j, and S_0 is the global ocean mean salinity set to 34.9 as in Hernández-Guerra and Talley (2016) and Talley (2008). Positive freshwater values are induced by higher evaporation than precipitation (freshwater flux from the ocean to the atmosphere). The freshwater results in 1992 (0.25 ± 0.02 FSv), 2003 (0.25 ± 0.02 FSv), 2009 (0.50 ± 0.03 FSv) and 2017 (0.34 ± 0.08 FSv) are all similar, but significantly different from the freshwater transport estimated in 2009 (Table 5). Overall, the freshwater results show an increase in net evaporation-precipitation from 2003 to 2009, that is nearly recovered in 2017.

Our temperature and freshwater transport results for 1992 are similar to the ones estimated by Wijffels et al. (2001) using WOCE data during the same year (0.75 ± 0.56 PW and 0.1 ± 0.1 FSv, respectively), as well as to the heat and freshwater transport (0.44 ± 0.25 PW and 0.06 FSv, respectively) estimated by Tsimplis et al. (1998).

10. Discussion and conclusions

The Deep Pacific MOC shows similar patterns in 1992, 2003, 2009 and 2017. The intensity of the overturning in 2009 (−11.6 ± 8.0 Sv) is weaker but not significantly different than in 1992 (−19.9 ± 7.4 Sv), 2003 (−15.5 ± 7.9 Sv), and 2017 (−18.4 ± 2.4 Sv). The net accumulated mass transport is not significantly different in the upper, deep, and bottom layers. At the same time, the "classic gyre" circulation pattern presented in years 1992, 2003, and 2017, characterized by a more zonal and regular shape, differs noticeably from the "bowed gyre" shape found in 2009. These noticeable differences in the circulation pattern are displayed in the three-layer sets of the accumulated mass transport at approximately 175°E, where a downwelling due to a Rossby wave as seen in SSHA, causes a strong poleward mass transport from the surface towards the bottom of the ocean. This southward mass transport in the Southwest Pacific Basin is then compensated at ~ 140°W by an equatorward flow across eastern Pacific in both the upper and deep layers, yet it is not found in the bottom layers. Moreover, after studying these

changes in the circulation pattern using four different ocean models (ECCO, MOM, SOSE, and GLORYS), we find that the "bowed gyre" shift presented in 2009 is not represented in any numerical modelling output. Thus, it cannot be inferred from the output of these models if the "bowed gyre" circulation pattern has been repeated in any other occasion in the South Pacific Ocean at 30°S through the different decades.

Furthermore, satellite altimetry suggests that changes in sea surface height anomaly in 1992 are associated with large-scale disturbances of 10–15 cm amplitude. These disturbances propagate slowly westward at roughly the speed of long baroclinic Rossby waves of ~ 3 cm/s, although the associated shifts in the circulation appear to be quasi-barotropic, extending to the bottom of the ocean. The disturbances seem to be generated in the eastern Pacific, between the East Pacific Rise and South America. Additionally, several apparent discontinuities along the westward propagating pathways obscure the propagating patterns of many Rossby waves. These discontinuities can be explained by the influence of the superimposed local factors also acting along the propagation track, including the effects of bathymetry and of atmosphere and ocean states, in addition to the remote forcing by the winds that first generated Rossby waves (Li et al., 2020; Maharaj et al., 2005; Perkins and Holbrook, 2001; Vivier et al., 1999). A downwelling Rossby wave caused an anomalously lower SSHA centered over the East Pacific Rise in 2003, and then propagated to the west arriving at the central Pacific between 160°W and 140°W when the cruise P06 in 2009 occurred. A baroclinic Rossby wave model provided a dynamical framework for a better understanding of the observed large-scale sea surface height signals. The variability of these signals in the South Pacific Ocean depends on the regional wind-stress curl forcing accumulated over the years prior to any specific time. The results from this model provide an explanation for the stronger poleward mass transport in the accumulated mass transport at approximately 175°E in 2009. As a result, changes due to the quasi-barotropic shift of the horizontal structure of the Pacific circulation within the different neutral density layers and years are independent from changes in the Deep Pacific MOC, extending into the deepest layers and including the Deep Western Boundary Current, which is part of the overturning circulation. As also noted in Hernández-Guerra and Talley (2016), this result suggests that the horizontal and overturning circulations are not coupled, and are affected by processes with independent time scales.

Finally, the "bowed gyre" circulation changes the temperature transport, as well as the freshwater transport across 32°S in the Pacific Ocean in 2009, as the estimated temperature and freshwater transports for this year are significantly different from the "classic gyre" years (0.42 ± 0.12 PW and 0.25 ± 0.02 FSv in 1992; 0.38 ± 0.12 PW and 0.25 ± 0.02 FSv in 2003; 0.16 ± 0.12 PW and 0.50 ± 0.03 FSv in 2009; 0.42 ± 0.12 PW and 0.34 ± 0.08 FSv in 2017). This is consistent with previous studies of Behrens et al. (2021), Bowen et al. (2017), Gnanaseelan and Vaid (2010), Polito and Liu (2003), Polito et al. (2000), that also reported Rossby waves, forced by wind-stress curl changes across the South Pacific Ocean, to be responsible for the change in the local heat and freshwater content of the water column.

In conclusion, the contribution of the downwelling Rossby waves not only provides a plausible explanation for the stronger poleward flow in the accumulated mass transport at approximately 175°E, which gave rise to the "bowed gyre" circulation pattern in 2009, but also for the modification in the local amount of heat and freshwater content of the water column north of 32°S in the Pacific Ocean in 2009, as the comprehensive analysis performed herein suggests.

Declaration of Competing Interest

The authors declare the following financial interests/personal relationships which may be considered as potential competing interests: Cristina Arumi-Planas reports financial support was provided by Agencia Canaria de Investigación, Innovación y Sociedad de la Información (ACIISI). Cristina Arumi-Planas reports a relationship with Agencia Canaria de Investigación, Innovación y Sociedad de la Información (ACIISI) that includes: employment.

Acknowledgments

This study was supported by the SAGA project (RTI2018-100844-B-C31) funded by the Ministerio de Ciencia, Innovación y Universidades of the Spanish Government. This article is a publication of the Unidad Océano y Clima from Universidad de Las Palmas de Gran Canaria, an R&D&I CSIC-associate unit. The wind data were collected from NCEP Reanalysis Derived data (http://www.eslr.noaa.gov/psd/). Hydrographic data were collected from the CCHDO website in the frame of International WOCE and GO-SHIP projects (https://cchdo.ucsd.edu/). We gratefully acknowledge the major efforts of the WOCE/GO-SHIP program's chief scientists that collected these transect data: H. L. Bryden, M. McCartney, J. Toole M. Fukasawa, S. Watanabe, Y. Yoshikawa, A. Macdonald, R. Curry, S. Mecking, and K. Speer. ECCO data are available for download at https://ecco.jpl.nasa.gov/. MOM data are available at https://www.gfdl.noaa.gov/mom-ocean-model/. SOSE data are available at http://sose.ucsd.edu. GLORYS data are available for download at https://resources.marine.copernicus.eu/. The SSHA data were collected from the Aviso database (http://las.aviso.oceanobs.com). The authors declare no competing interests. This work has been completed as part of C. Arumí-Planas work at IOCAG, in the doctoral program in Oceanography and Global Change. C. Arumí-Planas acknowledges the Agencia Canaria de Investigación, Innovación y Sociedad de la Información (ACIISI) grant program of "Apoyo al personal investigador en formación" TESIS2021010028. The authors are grateful to M. Cubas-Armas for her help with the data analysis and representation. Finally, C. Arumí-Planas gratefully acknowledges M. Casanova-Masjoan, who passed away in October 2020, for her optimism and positive energy which radiates through everyone who knew her, for her unconditional support and motivation since the first day working together, and for being one of the main reasons to always strive to do the best.

Appendix A

For a given station pair, the absolute geostrophic velocity (v_a), as a function of depth (z), is the sum of a relative velocity (v) and the velocity (b) at the reference level:

$$v_a(z) = v(z) + b$$

At each station pair, the inverse model finds the optimal solution for b. Firstly, the mass conservation is applied for the entire water column:

$$\iint \rho v_a dS = 0$$
$$\iint \rho (v + b) dS = 0 \tag{A.1a,b,c}$$
$$\sum_{j=1}^{N} \sum_{q=1}^{Q} \rho_{jq} \left(v_{jq} + b_j\right) a_{jq} = 0$$

where the area integral dS is over the entire section area, a_{jq} is the area for each station pair j and isoneutral layer q. In (A.1) and next equations, the term $\rho_{jq} v_{jq}$ is first summed over each 2 dbar interval within layer q. For the silicate conservation, these equations are multiplied with the silicate concentration. When mass transport is constrained to a particular non-zero value, M, (A.1c) becomes:

$$\sum_{j=1}^{N} \sum_{q=1}^{Q} \rho_{jq} \left(v_{jq} + b_j\right) a_{jq} = M \tag{A.1d}$$

where M is the mass transport constraints including the ITF and Bering Straight, and the limits for layers and station pairs are related to the constraint (Table 2). The total mass conservation is not exact because of the noise from eddies, internal waves, aliasing, measurements errors, etc.:

$$\sum_{j=1}^{N} \sum_{q=1}^{Q} \rho_{jq} b_j a_{jq} + n_{Total} = -\sum_{j=1}^{N} \sum_{q=1}^{Q} \rho_{jq} v_{jq} a_{jq} + M_{Total} \tag{A.2}$$

where n_{Total} is the noise.

The following equations, are obtained considering mass conservation in each layer q:

$$\sum_{j=1}^{N} \rho_{jq} b_j a_{jq} + n_q = -\sum_{j=1}^{N} \rho_{jq} v_{jq} a_{jq} + M_q \quad q = 1, 2, \cdots, Q \tag{A.3}$$

where M_q is the layer transport constraint and n_q is the layer noise. Next, this equation is written as:

$$\sum_{j=1}^{N} e_{jq} b_j + n_q = -y_q \quad q = 1, 2, \cdots, Q \tag{A.4}$$

where:

$$e_{jq} = \rho_{jq} a_{jq}$$
$$y_q = \sum_{j=1}^{N} \rho_{jq} v_{jq} a_{jq} - M_q \tag{A.5}$$

Then, the matrix equation is rewritten as:

$$\mathbf{A}\mathbf{b} + \mathbf{n} = -\mathbf{Y} \tag{A.6}$$

where $\mathbf{b}$ is an $N \times 1$ vector of the unknowns (reference velocities and adjustment of the Ekman transport), $\mathbf{A}$ is a $(Q+1) \times N$ matrix, $\mathbf{n}$ is a $(Q+1) \times 1$ vector, and $\mathbf{Y}$ is a $(Q+1) \times 1$ vector of values calculated from the CTD data and externally imposed mass transports. (Q is for the equations for each layer and the $+1$ is the equation for conservation of the whole water column.)

After that, the Ekman transport is included in the first layer and the total:

$$\begin{pmatrix} e_{11} & \cdots & e_{1n} & 1 \\ e_{21} & & e_{2n} & 0 \\ \vdots & \ddots & \vdots & \vdots \\ e_{q,1} & & e_{q,n} & 0 \\ e_{q+1,1} & \cdots & e_{q+1,n} & 1 \end{pmatrix} \begin{pmatrix} b_1 \\ \vdots \\ b_n \\ \Delta T_{Ek} \end{pmatrix} = \begin{pmatrix} y_1 + T_{Ek} \\ y_2 \\ \vdots \\ y_q \\ y_{q+1} + T_{Ek} \end{pmatrix}$$

To solve this matrix, the Gauss–Markov estimator is applied (Wunsch, 1996), as in Hernández-Guerra and Talley (2016).

For this inverse model, 7 different constraints are applied, which correspond to mass and silica conservation for the Pacific Ocean, and 5 additional mass transport constraints (boundary currents and deep flows) (Table 2).

References

Adcroft, A., Anderson, W., Balaji, V., Blanton, C., Bushuk, M., Dufour, C.O., Dunne, J.P., Griffies, S.M., Hallberg, R., Harrison, M.J., Held, I.M., Jansen, M.F., John, J.G., Krasting, J.P., Langenhorst, A.R., Legg, S., Liang, Z., McHugh, C., Radhakrishnan, A., Reichl, B.G., Rosati, T., Samuels, B.L., Shao, A., Stouffer, R., Winton, M., Wittenberg, A.T., Xiang, B., Zadeh, N., Zhang, R., 2019. The GFDL Global Ocean and Sea Ice Model OM4.0: Model Description and Simulation Features. J. Adv. Model. Earth Syst. 11 (10), 3167–3211. https://doi.org/10.1029/2019MS001726.

Archer, M.R., Roughan, M., Keating, S.R., Schaeffer, A., 2017. On the Variability of the East Australian Current: Jet Structure, Meandering, and Influence on Shelf Circulation. J. Geophys. Res. Oceans 122 (11), 8464–8481. https://doi.org/10.1002/2017JC013097.

Behrens, E., Hogg, A.M., England, M.H., Bostock, H., 2021. Seasonal and Interannual Variability of the Subtropical Front in the New Zealand Region. J. Geophys. Res. Oceans 126 (2). https://doi.org/10.1029/2020JC016412.

Bowen, M., Markham, J., Sutton, P., Zhang, X., Wu, Q., Shears, N.T., Fernandez, D., 2017. Interannual Variability of Sea Surface Temperature in the Southwest Pacific and the Role of Ocean Dynamics. J. Clim. 30 (18), 7481–7492. https://doi.org/10.1175/JCLI-D-16-0852.1.

Brink, K.H., Robinson, A.R. (Eds.)., 2005. The Global Coastal Ocean-Regional Studies and Syntheses, Vol. 11. Harvard University Press.

Callahan, J.E., 1972. The structure and circulation of deep water in the Antarctic. Deep Sea Res. Oceanogr. Abstr. 19 (8), 563–575. https://doi.org/10.1016/0011-7471(72)90040-X.

Casanova-Masjoan, M., Joyce, T., Pérez-Hernández, M.D., Vélez-Belchí, P., Hernández-Guerra, A., 2018. Changes across 66°W, the Caribbean Sea and the Western boundaries of the North Atlantic Subtropical Gyre. Prog. Oceanogr. 168, 296–309. https://doi.org/10.1016/j.pocean.2018.09.013.

Casanova-Masjoan, M., Pérez-Hernández, M.D., Vélez-Belchí, P., Cana, L., Hernández-Guerra, A., 2020. Variability of the Canary Current Diagnosed by Inverse Box Models. J. Geophys. Res. Oceans 125 (8). https://doi.org/10.1029/2020JC016199.

Chaigneau, A., Dominguez, N., Eldin, G., Vasquez, L., Flores, R., Grados, C., Echevin, V., 2013. Near-coastal circulation in the Northern Humboldt Current System from shipboard ADCP data. J. Geophys. Res. Oceans 118 (10), 5251–5266. https://doi.org/10.1002/jgrc.20328.

Chapman, P., 1998. The World Ocean Circulation Experiment (WOCE). Mar. Technol. Soc. J. 32 (3), 23.

Chelton, D.B., Schlax, M.G., 1996. Global observations of oceanic Rossby waves. Science 272 (5259), 234–238.

Chiswell, S.M., Toole, J., Church, J., 1997. Transports across the Tasman Sea from WOCE repeat sections: the East Australian Current 1990–94. New Zealand J. Mar. Freshwater Res. 31 (4), 469–475.

Comas-Rodríguez, I., Hernández-Guerra, A., McDonagh, E.L., 2010. Referencing geostrophic velocities using ADCP data at 24.5°N (North Atlantic). Sci. Mar. 74 (2), 331–338. https://doi.org/10.3989/scimar.2010.74n2331.

Drévillon, M., Bahurel, P., Bazin, D., Benkiran, M., Beuvier, J., Crosnier, L., Drillet, Y., Durand, E., Fabardines, M., Garcia Hermosa, I., Giordan, C., Gutknecht, E., Hernandez, F., Law Chune, S., Le Traon, Pierre-Yves., Lellouche, J-M., Levier, B., Melet, A., Obaton, D., Paul, J., Peltier, M., Peyrot, D., Rémy, E., von Schuckmann, K., Tomas-Courcoux, C., 2018. Learning about Copernicus Marine Environment Monitorin Service "CMEMS": A Practical Introduction to the Use of the European Operational Oceanography Service. New Frontiers in Operational Oceanography 695–712.

Emery, W.J., 2001. Water types and water masses. Encyclopedia Ocean Sci. 6, 3179–3187.

Emery, W.J., Meincke, J., 1986. Global water masses-cummary and review. Oceanol. Acta 9 (4), 383–391.

Forget, G., Campin, J.-M., Heimbach, P., Hill, C.N., Ponte, R.M., Wunsch, C., 2015. ECCO version 4: An integrated framework for non-linear inverse modeling and global ocean state estimation. Geosci. Model Dev. 8 (10), 3071–3104. https://doi.org/10.5194/gmd-8-3071-2015.

Fu, L., Qiu, B., 2002. Low-frequency variability of the North Pacific Ocean : The roles of boundary- and wind-driven baroclinic Rossby waves. J. Geophys. Res. 107 (C12), 3220. https://doi.org/10.1029/2001JC001131.

Fukumori, I., Wang, O., Fenty, I., Forget, G., Heimbach, P., Ponte, R.M., 2017. ECCO Version 4 Release 3, 2(2015), 10. https://doi.org/1721.1/110380.

Ganachaud, A., 2003. Large-scale mass transports, water mass formation, and diffusivities estimated from World Ocean Circulation Experiment (WOCE) hydrographic data. J. Geophys. Res. 108 (C7) https://doi.org/10.1029/2002jc001565.

Ganachaud, A., Wunsch, C., 2000. Improved estimates of global ocean circulation, heat transport and mixing from hydrographic data. Nature 408 (6811), 453–457.

Ganachaud, A., Wunsch, C., 2003. Large-Scale Ocean Heat and Freshwater Transports during the World Ocean Circulation Experiment. J. Clim. 16(4), 696–705. https://doi.org/https://doi.org/10.1175/1520-0442(2003)016<0696:LSOHAF>2.0.CO;2.

Gnanaseelan, C., Vaid, B.H., 2010. Interannual variability in the Biannual Rossby waves in the tropical Indian Ocean and its relation to Indian Ocean Dipole and El Niño forcing. Ocean Dyn. 60 (1), 27–40.

Godfrey, J.S., 1989. A Sverdrup model of the depth-integrated flow for the world ocean allowing for island circulations. Geophys. Astrophys. Fluid Dyn. 45 (1-2), 89–112.

Gordon, A.L., 1986. Interocean exchange of thermocline water. J. Geophys. Res. 91 (C4), 5037–5046.

Hamon, B.V., Tranter, D.J., 1971. East Australian Current. Aust. Nat. History 17 (4), 129–133. hdl.handle.net/102.100.100/317290?index=1.

Hernández-Guerra, A., Espino-Falcón, E., Vélez-Belchí, P., Dolores Pérez-Hernández, M., Martínez-Marrero, A., Cana, L., 2017. Recirculation of the Canary Current in fall 2014. J. Mar. Syst. 174, 25–39.

Hernández-Guerra, A., Fraile-Nuez, E., López-Laatzen, F., Martínez, A., Parrilla, G., Vélez-Belchí, P., 2005. Canary Current and North Equatorial Current from an inverse box model. J. Geophys. Res. Oceans 110 (C12). https://doi.org/10.1029/2005JC003032.

Hernández-Guerra, A., Joyce, T.M., Fraile-Nuez, E., Vélez-Belchí, P., 2010. Using Argo data to investigate the Meridional Overturning Circulation in the North Atlantic. Deep Sea Res. Part I: Oceanogr. Res. Papers 57 (1), 29–36. https://doi.org/10.1016/j.dsr.2009.10.003.

Hernández-Guerra, A., Pelegrí, J.L., Fraile-Nuez, E., Benítez-Barrios, V.M., Emelianov, M., Pérez-Hernández, M.D., Vélez-Belchí, P., 2014. Meridional Overturning Transports at 7.5N and 24.5 N in the Atlantic Ocean during 1992–93 and 2010–11. Prog. Oceanogr. 128, 98–114. https://doi.org/10.1016/j.pocean.2014.08.016.

Hernández-Guerra, A., Talley, L.D., 2016. Meridional overturning transports at 30°S in the Indian and Pacific Oceans in 2002–2003 and 2009. Prog. Oceanogr. 146, 89–120. https://doi.org/10.1016/j.pocean.2016.06.005.

Hernández-Guerra, A., Talley, L.D., Pelegrí, J.L., Vélez-Belchí, P., Baringer, M.O., Macdonald, A.M., McDonagh, E.L., 2019. The upper, deep, abyssal and overturning circulation in the Atlantic Ocean at 30°S in 2003 and 2011. Prog. Oceanogr. 176, 102136. https://doi.org/10.1016/j.pocean.2019.102136.

Hill, K.L., Rintoul, S.R., Oke, P.R., Ridgway, K., 2010. Rapid response of the East Australian Current to remote wind forcing: The role of barotropic-baroclinic interactions. J. Mar. Res. 68 (3), 413–431. https://doi.org/10.1357/002224010794657218.

Huyer, A., Smith, R.L., Paluszkiewicz, T., 1987. Coastal upwelling off Peru during normal and El Niño times. J. Geophys. Res. Oceans 92 (C13), 14297–14307.

Jackett, D.R., Mcdougall, T.J., 1997. A neutral density variable for the world's oceans. J. Phys. Oceanogr., 27(2), 237–263. https://doi.org/10.1175/1520-0485(1997)027<0237:ANDVFT>2.0.CO;2.

Johnson, C.R., Banks, S.C., Barrett, N.S., Cazassus, F., Dunstan, P.K., Edgar, G.J., Frusher, S.D., Gardner, C., Haddon, M., Helidoniotis, F., Hill, K.L., Holbrook, N.J., Hosie, G.W., Last, P.R., Ling, S.D., Melbourne-Thomas, J., Miller, K., Pecl, G.T., Richardson, A.J., Ridgway, K.R., Rintoul, S.R., Ritz, D.A., Ross, D.J., Sanderson, J.C., Shepherd, S.A., Slotwinski, A., Swadling, K.M., Taw, N., 2011. Climate change cascades: Shifts in oceanography, species' ranges and subtidal marine community dynamics in eastern Tasmania. J. Exp. Mar. Biol. Ecol. 400 (1-2), 17–32. https://doi.org/10.1016/j.jembe.2011.02.032.

Joyce, T.M., Hernandez-Guerra, A., Smethie, W.M., 2001. Zonal circulation in the NW Atlantic and Caribbean from a meridional World Ocean Circulation Experiment hydrographic section at 66 W. J. Geophys. Res. Oceans 106 (C10), 22095–22113.

Kalnay, E., Kanamitsu, M., Kistler, R., Collins, W., Deaven, D., Gandin, L., Joseph, D. (1996). The NCEP/NCAR 40-Year Reanalysis Project. Bull. Am. Meteorol. Soc. 77(3), 437–471. https://doi.org/10.1175/1520-0477(1996)077<0437:TNYRP>2.0.CO;2.

Katsumata, K., Fukasawa, M., 2011. Changes in meridional fluxes and water properties in the Southern Hemisphere subtropical oceans between 1992/1995 and 2003/2004. Prog. Oceanogr. 89 (1–4), 61–91. https://doi.org/10.1016/j.pocean.2010.12.008.

Kawano, T., Fukasawa, M., Kouketsu, S., Uchida, H., Doi, T., Kaneko, I., Aoyama, M., Schneider, W., 2006. Bottom water warming along the pathway of lower circumpolar deep water in the Pacific Ocean. Geophys. Res. Lett. 33 (23) https://doi.org/10.1029/2006GL027933.

Kerry, C., Roughan, M., 2020. Downstream Evolution of the East Australian Current System: Mean Flow, Seasonal, and Intra-annual Variability. J. Geophys. Res. Oceans 125 (5), 1–28. https://doi.org/10.1029/2019JC015227.

Knauss, J.A., 1962. On some aspects of the deep circulation of the Pacific. J. Geophys. Res. 67 (10), 3943–3954. https://doi.org/10.1029/JZ067i010p03943.

Li, Z., Holbrook, N.J., Zhang, X., Oliver, E.C.J., Cougnon, E.A., 2020. Remote Forcing of Tasman Sea Marine Heatwaves. J. Clim. 33 (12), 5337–5354. https://doi.org/10.1175/JCLI-D-19-0641.1.

Lumpkin, R., Speer, K., 2007a. Global Ocean Meridional Overturning. J. Phys. Oceanogr. 37 (10), 2550–2562. https://doi.org/10.1175/JPO3130.1.

Lumpkin, R., Speer, K., 2007b. Interocean exchange of thermocline water. J. Phys. Oceanogr. 37 (10), 2550–2562.

Macdonald, A.M., Mecking, S., Robbins, P.E., Toole, J.M., Johnson, G.C., Talley, L., Cook, M., Wijffels, S.E., 2009. The WOCE-era 3-D Pacific Ocean circulation and heat budget. Prog. Oceanogr. 82 (4), 281–325. https://doi.org/10.1016/j.pocean.2009.08.002.

Macdonald, A.M., Wunsch, C., 1996. An estimate of global ocean circulation and heat fluxes. Nature 382 (6590), 436–439.

Maharaj, A.M., Cipollini, P., Holbrook, N.J., 2005. Observed variability of the South Pacific westward sea level anomaly signal in the presence of bottom topography. Geophys. Res. Lett. 32 (4), L04611. https://doi.org/10.1029/2004GL020966.

Mata, M.M., Tomczak, M., Wijffels, S., Church, J.A., 2000. East Australian Current volume transports at 30°S: Estimates from the World Ocean Circulation Experiment hydrographic sections PR11/P6 and the PCM3 current meter array. J. Geophys. Res. Oceans 105 (C12), 28509–28526. https://doi.org/10.1029/1999jc000121.

Mazloff, M., & (Eds.)., N. C. for A. R. S. (n.d.). The Climate Data Guide: Southern Ocean State Estimate (SOSE). Retrieved from https://climatedataguide.ucar.edu/climate-data/southern-ocean-state-estimate-sose.

McCarthy, M.C., Talley, L.D., Roemmich, D., 2000. Seasonal to interannual variability from expendable bathythermograph and TOPEX/Poseidon altimeter data in the South Pacific subtropical gyre. J. Geophys. Res. Oceans 105 (C8), 19535–19550.

Montes, I., Colas, F., Capet, X., Schneider, W., 2010. On the pathways of the equatorial subsurface currents in the eastern equatorial Pacific and their contributions to the Peru-Chile Undercurrent. J. Geophys. Res. Oceans 115 (C9). https://doi.org/10.1029/2009JC005710.

Moore, M.I., Wilkin, J.L., 1998. Variability in the South Pacific Deep Western Boundary Current from current meter observations and a high-resolution global model. J. Geophys. Res. Oceans 103 (C3), 5439–5457. https://doi.org/10.1029/97jc03207.

Mulhearn, P.J., 1987. The Tasman Front: A study using satellite infrared imagery. J. Phys. Oceanogr. 17 (8), 1148–1155.

Neshyba, S., 1979. On the southernmost extension of the Peru-Chile Undercurrent. Deep-Sea Res. Part A. Oceanogr. Res. Papers 26 (12), 1387–1393.

Oke, P.R., Roughan, M., Cetina-Heredia, P., Pilo, G.S., Ridgway, K.R., Rykova, T., Archer, M.R., Coleman, R.C., Kerry, C.G., Rocha, C., Schaeffer, A., Vitarelli, E., 2019. Revisiting the circulation of the East Australian Current: Its path, separation, and eddy field. Prog. Oceanogr. 176, 102139. https://doi.org/10.1016/j.pocean.2019.102139.

Pérez-Hernández, M.D., Hernández-Guerra, A., Fraile-Nuez, E., Comas-Rodríguez, I., Benítez-Barrios, V.M., Domínguez-Yanes, J.F., Vélez-Belchí, P., De Armas, D., 2013. The source of the Canary Current in fall 2009. J. Geophys. Res. Oceans 118 (6), 2874–2891. https://doi.org/10.1002/jgrc.20227.

Perkins, M.L., Holbrook, N.J., 2001. Can Pacific Ocean thermocline depth anomalies be simulated by a simple linear vorticity model? J. Phys. Oceanogr. 31, 1786–1806. https://doi.org/10.1175/1520-0485(2001)031,1786:CPOTDA.2.0.CO;2.

Polito, P.S., Liu, W.T., 2003. Global characterization of Rossby waves at several spectral bands. J. Geophys. Res. 108 (C1), 3018. https://doi.org/10.1029/2000JC000607.

Polito, P.S., Sato, O.T., Liu, W.T., 2000. Characterization and validation of the heat storage variability from TOPEX / Poseidon at four oceanographic sites. J. Geophys. Res. 105 (C7), 16911–16921.

Purkey, S.G., Johnson, G.C., Talley, L.D., Sloyan, B.M., Wijffels, S.E., Smethie, W., Mecking, S., Katsumata, K., 2019. Unabated bottom water warming and freshening in the South Pacific Ocean. J. Geophys. Res. Oceans 124 (3), 1778–1794. https://doi.org/10.1029/2018JC014775.

Reid, J.L., 1997. On the total geostrophic circulation of the Pacific Ocean: flow patterns, tracers, and transports. Prog. Oceanogr. 39 (4), 263–352. https://doi.org/10.1016/S0079-6611(97)00012-8.

Ribbat, N., Roughan, M., Powell, B., Rao, S., Kerry, C.G., 2020. Transport variability over the Hawkesbury Shelf (31.5–34.5°S) driven by the East Australian Current. PLOS ONE, 15(11), e0241622. https://doi.org/10.1371/journal.pone.0241622.

Ridgway, K.R., 2007. Long-term trend and decadal variability of the southward penetration of the East Australian Current. Geophys. Res. Lett. 34 (13), 345–365. https://doi.org/10.1029/2007GL030393.

Ridgway, K.R., Godfrey, J.S., 1994. Mass and heat budgets in the East Australian Current: A direct approach. J. Geophys. Res. Oceans 99 (C2), 3231–3248.

Ridgway, K.R., Godfrey, J.S., 1997. Seasonal cycle of the East Australian Current. J. Geophys. Res. 102 (C10), 22921–22936.

Robbins, P.E., Toole, J.M., 1997. The dissolved silica budget as a constraint on the meridional overturning circulation of the Indian Ocean. Deep Sea Res. Part I: Oceanogr. Res. Papers 44 (5), 879–906. https://doi.org/10.1016/S0967-0637(96)00126-4.

Roemmich, D., Wunsch, C., 1985. Two transatlantic sections: meridional circulation and heat flux in the subtropical North Atlantic Ocean. Deep Sea Res. Part A. Oceanogr. Res. Papers 32 (6), 619–664. https://doi.org/10.1016/0198-0149(85)90070-6.

Schmitz, W.J., 1995. On the interbasin-scale thermohaline circulation. Rev. Geophys. 33 (2), 151. https://doi.org/10.1029/95RG00879.

Schulze Chretien, L.M., Speer, K., 2019. A deep eastern boundary current in the Chile Basin. J. Geophys. Res. Oceans 124 (1), 27–40. https://doi.org/10.1029/2018JC014400.

Shaffer, G., Hormazabal, S., Pizarro, O., Ramos, M., 2004. Circulation and variability in the Chile Basin. Deep Sea Res. Part I: Oceanogr. Res. Papers 51 (10), 1367–1386.

Shaffer, G., Hormazabal, S., Pizarro, O., Salinas, S., 1999. Seasonal and interannual variability of currents and temperature off central Chile. J. Geophys. Res. Oceans 104 (C12), 29951–29961.

Silva, N., Rojas, N., Fedele, A., 2009. Water masses in the Humboldt Current System: Properties, distribution, and the nitrate deficit as a chemical water mass tracer for Equatorial Subsurface Water off Chile. Deep-Sea Res. 56 (16), 1004–1020. https://doi.org/10.1016/j.dsr2.2008.12.013.

Sloyan, B.M., Ridgway, K.R., Cowley, R., 2016. The East Australian Current and Property Transport at 27°S from 2012 to 2013. J. Phys. Oceanogr. 46 (3), 993–1008. https://doi.org/10.1175/JPO-D-15-0052.1.

Sprintall, J., Tomczak, M., 1993. On the formation of Central Water and thermocline ventilation in the southern hemisphere. Deep-Sea Res., I 40 (4), 827–848.

Stramma, L., Johnson, G.C., Firing, E., Schmidtko, S., 2010. Eastern Pacific oxygen minimum zones: Supply paths and multidecadal changes. J. Geophys. Res. 115 (C9) https://doi.org/10.1029/2009JC005976.

Strub, P.T., Mesias, J.M., Montecino, V., Ruttlant, J., Salinas, S., 1998. Coastal ocean circulation off western South America. In: Brink, K.H., Robinson, A.R. (Eds.), The Sea, pp. 273–313.

Sverdrup, H.U., 1947. Wind-driven currents in a baroclinic ocean; with application to the equatorial currents of the eastern Pacific. Proc. Natl. Acad. Sci. USA 33 (11), 318–326.

Talley, L.D., 2003. Shallow, intermediate, and deep overturning components of the global heat budget. J. Phys. Oceanogr. 33 (3), 530–560.

Talley, L.D., 2008. Freshwater transport estimates and the global overturning circulation: sallow, deep and throughflow components. Prog. Oceanogr. 78, 257–303.

Talley, L.D., Feely, R.A., Sloyan, B.M., Wanninkhof, R., Baringer, M.O., Bullister, J.L., Carlson, C.A., Doney, S.C., Fine, R.A., Firing, E., Gruber, N., Hansell, D.A., Ishii, M., Johnson, G.C., Katsumata, K., Key, R.M., Kramp, M., Langdon, C., Macdonald, A.M., Mathis, J.T., McDonagh, E.L., Mecking, S., Millero, F.J., Mordy, C.W., Nakano, T., Sabine, C.L., Smethie, W.M., Swift, J.H., Tanhua, T., Thurnherr, A.M., Warner, M.J., Zhang, J.-Z., 2016. Changes in ocean heat, carbon content, and ventilation: A review of the first decade of GO-SHIP global repeat hydrography. Ann. Rev. Mar. Sci. 8 (1), 185–215. https://doi.org/10.1146/annurev-marine-052915-100829.

Talley, L.D., Pickard, G.L., Emery, W.J., Swift, J.H., 2011. Descriptive Physical Oceanography: An Introduction (Sixth). B: Elsevier Ltd.

Talley, L.D., Reid, J.L., Robbins, P.E., 2003. Data-based meridional overturning streamfunctions for the global ocean. J. Clim. 16 (19), 3213–3226. https://doi.org/10.1175/1520-0442(2003)016<3213:DMOSFT>2.0.CO;2.

Talley, L.D., Sprintall, J., 2005. Deep expression of the Indonesian Throughflow: Indonesian intermediate water in the South Equatorial Current. J. Geophys. Res. Oceans 110 (C10). https://doi.org/10.1029/2004JC002826.

Tomczak, M., Godfrey, J.S., 1994. Regional oceanography: an introduction. Pergamon, Tarrytown, N. Y.

Tsimplis, M.N., Bacon, S., Bryden, H.L., 1998. The circulation of the subtropical South Pacific derived from hydrographic data. J. Geophys. Res. Oceans 103 (C10), 21443–21468.

Tsuchiya, M., 1990. Flow path of the Antarctic Intermediate Water in the western equatorial South Pacific Ocean. Deep-Sea Res. 33, S273–S279. https://doi.org/10.1016/S0198-0149(12)80013-6.

Tsuchiya, M., Talley, L.D., 1996. Water-property distributions along an eastern Pacific hydrographie section at 135W. J. Mar. Res. 54 (3), 541–564. https://doi.org/10.1357/0022240963213583.

Tsuchiya, M., Talley, L.D., 1998. A Pacific hydrographic section at 88° W: Water-property distribution. J. Geophys. Res. 103 (C6), 12899–12918.

Tsujino, H., Urakawa, L.S., Griffies, S.M., Danabasoglu, G., Adcroft, A.J., Amaral, A.E., Arsouze, T., Bentsen, M., Bernardello, R., Böning, C.W., Bozec, A., Chassignet, E.P., Danilov, S., Dussin, R., Exarchou, E., Fogli, P.G., Fox-Kemper, B., Guo, C., Ilicak, M., Iovino, D., Kim, W.M., Koldunov, N., Lapin, V., Li, Y., Lin, P., Lindsay, K., Liu, H., Long, M.C., Komuro, Y., Marsland, S.J., Masina, S., Nummelin, A., Rieck, J.K., Ruprich-Robert, Y., Scheinert, M., Sicardi, V., Sidorenko, D., Suzuki, T., Tatebe, H., Wang, Q., Yeager, S.G., Yu, Z., 2020. Evaluation of global ocean–sea-ice model simulations based on the experimental protocols of the Ocean Model Intercomparison Project phase 2 (OMIP-2). Geosci. Model Dev. 13 (8), 3643–3708. https://doi.org/10.5194/gmd-13-3643-202010.5194/gmd-13-3643-2020-supplement.

Vélez-Belchí, P., Pérez-Hernández, M.D., Casanova-Masjoan, M., Cana, L., Hernández-Guerra, A., 2017. On the seasonal variability of the Canary Current and the Atlantic Meridional Overturning Circulation. J. Geophys. Res. Oceans 122 (6), 4518–4538.

Vergara, O.A., Echevín, V., Sepúlveda, H.H., Colas, F., Quiñones, R.A., 2016. Modelling the seasonal dynamics of the Peru-Chile Undercurrent off Central Chile (30–40°S). Cont. Shelf Res. 123, 61–79. https://doi.org/10.1016/j.csr.2016.04.001.

Vivier, F., Kelly, K.A., Thompson, L., 1999. Contributions of wind forcing, waves, and surface heating to sea surface height observations in the Pacific Ocean. J. Geophys. Res. Oceans 104 (C9), 20767–20788. https://doi.org/10.1029/1999JC900096.

Whitworth, T.I., Warren, B.A., Nowlin Jr, W.D., Rutz, S.B., Pillsbury, R.D., Moore, M.I., 1999. On the deep western-boundary current in the Southwest Pacific Basin. Prog. Oceanogr. 43 (1), 1–54.

Wijffels, S.E., Hall, M.M., Joyce, T., Torres, D.J., Hacker, P., Firing, E., 1998. Multiple deep gyres of the western North Pacific: A WOCE section along 149°E. J. Geophys. Res. Oceans 103 (C6), 12985–13009. https://doi.org/10.1029/98JC01016.

Wijffels, S.E., Toole, J.M., Davis, R., 2001. Revisiting the South Pacific subtropical circulation: A synthesis of World Ocean Circulation Experiment observations along 32°S. J. Geophys. Res. Oceans 106 (C9), 19481–19513. https://doi.org/10.1029/1999jc000118.

Wooster, W.S., Reid, J.L., 1963. 11. Eastern Boundary Currents. In: The Composition of Sea-water: Comparative and Descriptive Oceanography, 2, pp. 253–280).

Wu, L., Cai, W., Zhang, L., Nakamura, H., Timmermann, A., Joyce, T., McPhaden, M.J., Alexander, M., Qiu, B., Visbeck, M., Chang, P., Giese, B., 2012. Enhanced warming over the global subtropical western boundary currents. Nat. Clim. Change 2 (3), 161–166. https://doi.org/10.1038/nclimate1353.

Wunsch, C., 1978. North-Atlantic general circulation west of 50°W determined by inverse methods. Rev. Geophys. 16 (4), 583–620. https://doi.org/10.1029/RG016i004p00583.

Wunsch, C. (Ed.), 1996. The Ocean Circulation Inverse Problem. Cambridge University Press.

Wunsch, C., Hu, D., Grant, B., 1983. Mass, heat, salt and nutrient fluxes in the South Pacific Ocean. J. Phys. Oceanogr. 13(5), 725–753. Doi: 10.1175/1520-0485(1983)013<0725:MHSANF>2.0.CO;2.

Wyrtki, K., 1967. Circulation and water masses in the eastern equatorial Pacific Ocean. Int. J. Oceanol. & Limnol. 1 (2), 117–147.

Wyrtki, K., 1975. Fluctuations of the dynamic topography in the Pacific Ocean. J. Phys. Oceanogr. 5 (3), 450–459. https://doi.org/10.1175/1520-0485(1975)005<0450:FOTDTI>2.0.CO;2.